REGULATORY CONSEQUENCES OF BANDPASS FEEDBACK IN A BACTERIAL PHOSPHORELAY

Thesis by

Shaunak Sen

In Partial Fulfillment of the Requirements

for the Degree of

Doctor of Philosophy

California Institute of Technology

Pasadena, California

2011

(Defended May 5, 2011)

Acknowledgements

I want to thank my advisor, Michael Elowitz, for providing invaluable guidance and support during the research period, and for suggesting the problems addressed in this thesis.

Richard Murray has been immensely helpful with his feedback at key points during the inception and execution of the thesis research.

Jordi Garcia-Ojalvo at UPC, Terrassa, deserves a lot of credit for providing starting points to compute dynamical behavior in cells, for pointing out how these computations can serve as organizational principles to understand cellular behavior, and for hosting me in his group.

I also want to thank John Doyle for serving on my thesis committee, and helping me connect the thesis work with a broader dynamics/ control perspective.

All of their groups have been extremely helpful in numerous ways. Specifically, I want to thank Chiraj Dalal, Joe Levine, Jon Young and James Locke, for critical readings of major parts of this thesis, and for sharing their technical expertise.

Finally, I want to acknowledge financial support, through the Poincare Fellowship, from the Betty and Gordon Moore Foundation, Caltech.

Abstract

Under conditions of nutrient limitation, *Bacillus subtilis* cells terminally differentiate into a dormant spore state. Progression to sporulation is controlled by a genetic circuit structured as a phosphorelay embedded in multiple transcriptional feedback loops, and which is used to activate the master regulator Spo0A by phosphorylation. These transcriptional regulatory interactions are "bandpass"-like, in the sense that activation occurs within a limited band of Spo0A∼P concentrations, and have recently been shown to pulse in a cell-cycle-dependent fashion. Additionally, the core phosphorelay is an architectural variant of the canonical two-component signaling system, which allows signal integration from a larger number of inputs, including two types of phosphatases that act on different protein components. However, the impact of these pulsed bandpass interactions on the circuit dynamics preceding sporulation and the utility of two types of phosphatases remains unclear. In order to address these questions, we measured key features of the bandpass interactions at the single-cell level and analyzed them in the context of a simple mathematical model. The model predicted the emergence of a delayed phase shift between the pulsing activity of the different sporulation genes, as well as the existence of a stable state, with elevated Spo0A activity but no sporulation, embedded within the dynamical structure of the system. To test the model, we used time-lapse fluorescence microscopy to measure dynamics of single cells initiating sporulation. We observed the delayed phase shift emerging during the progression to sporulation, while a re-engineering of the sporulation circuit revealed behavior resembling the predicted additional state. The core phosphorelay model also showed a post-translational bandpass response, and we find that the two types of phosphatases can independently tune the two bandpass thresholds. These results show that periodically-driven bandpass feedback loops can give rise to complex dynamics in the progression towards sporulation, and that similar inputs can tune different response features.

Contents

Acknowledgements **iii**

Abstract **iv**

Contents **v**

1 Introduction **1**

1.1 Genetic Circuits and Single-Cell Dynamics 1

1.2 Phosphorelay: Circuit Structure and Signaling Architecture 2

1.3 Thesis Overview 6

2 Dynamical Implications of Phosphorelay Circuit Structure **10**

2.1 Transcriptional Bandpasses 10

2.2 Post-Translational Bandpass 14

2.3 Delayed Phase Shift 17

2.4 Alternate Cellular State 22

2.5 Interplay between Periodic Input and Circuit Dynamics 26

3 Functional Potential of the Core Phosphorelay Architecture **28**

3.1 Independent Tuning of Bandpass Thresholds 28

3.2 Linear Amplifier-like Responses 37

3.2.1 Two-Component System 40

3.2.2 Phosphorelay 42

3.3 Analogies to Electrical Circuits 49

4 Conclusion **51**

4.1 Summary of Contributions 51

4.2 Future Work 52
4.2.1 Systematic perturbation of bandpass responses in sporulation progression 52
4.2.2 Role of temporally ordered gene expression in formation of the asymmetric septum 53
4.2.3 Power consumption in two-component signaling architectures 54

A Materials and Methods **55**

B Movie Protocols **60**

C Analysis of Models **64**

Bibliography **73**

Chapter 1

Introduction

Many instances of temporal patterns are found in biology. Examples span all levels of biological hierarchy, and recent studies include investigations of fluctuations within individual protein molecules [39], oscillations of protein concentrations inside cells [38], initiation and propagation of action potentials in specialized cells like neurons [4, 14], formation of spatial patterns of cells during organ development [49], spatiotemporal rhythms inside organs like the heart [21, 36], and population growth of species within ecosystems [3].

1.1 Genetic Circuits and Single-Cell Dynamics

As the smallest living unit that can self-replicate, the cell occupies a special position in the hierarchy of the biological systems. Indeed, living organisms can be unicellular, like bacteria or yeast, or multicellular, like plants and animals. In addition to self-replication, cells can exhibit other behaviors [1, 8–10, 64]: generating energy by metabolizing nutrients, searching for nutrients, maintaining circadian rhythms, responding to environmental changes. Many of these processes are inherently dynamical, and are observed to function reliably in a range of different environmental conditions. These behaviors are programmed inside cells in the form of their DNA, in structural units called genes. Genes produce proteins, which act individually or in combination with other proteins as molecular machines to perform specific functions: replicating DNA, digesting sugar, forming motors, regulating gene expression, modifying protein activity. Interactions between genes and proteins, called genetic circuits, form the basis of cellular behavior.

Reducing cellular behavior to interactions within their underlying genetic circuits is a fundamental problem in cell biology. While previous attempts to use mathematical mod-

els were considerably successful in shedding light on this problem [32, 40], they were only indirectly linked to molecular mechanisms, and also not equipped with direct methods to test model assumptions and predictions. However, two major developments in recent times have the potential to significantly overcome these limitations: First, significant effort has been invested in identification of genes, proteins, and their interactions, and this process has only accelerated over the last few years. These projects have uncovered a complex network of interactions in genetic circuits, rivaling the complexity in advanced engineering networks. Second, new tools like fluorescent proteins have been combined with time-lapse microscopy methods to usher in a new era of quantitative temporal measurements in individual cells, or movies. Such movies can provide measurements at the level of individual cells, revealing features that may have been previously averaged over in cell populations. Further, they have the potential to highlight the subset of regulatory links that are active during a cellular process, and provide a direct means to verify temporal patterns that typically arise from mathematical models. Efforts to combine these advances in genetic circuit identification and measurement techniques with mathematical models have the potential to offer more complete solutions to this problem. Additionally, such models can offer succinct summaries of cellular behavior, serving to highlight unifying features across other biological and engineering processes.

Recent instances of such efforts include investigations of bistability in cellular signaling [42], excitability in transient differentiation [58, 59], limit cycles underlying circadian rhythms [52], integral feedback control in bacterial signaling [54, 67], regulatory mechanisms during heat shock responses [18], pattern formation during embryonic segmentation [50], and spatiotemporal oscillations regulating cell division [30]. Complementarily, they can also serve as computational design aids in synthesizing genetic circuits to generate new and useful cellular dynamics, like switches [25], clocks [20, 57], and patterns [6, 16].

1.2 Phosphorelay: Circuit Structure and Signaling Architecture

Terminal differentiation is an important type of cellular behavior that recurs in numerous biological contexts. Examples in eukaryotes include neuron development [27], maturation of *Xenopus* oocytes [66], cell death by apoptosis [55], meiosis in yeast [41], and flowering

in plants [63]. Despite significant effort on identifying the molecular circuit controlling these processes, it often remains unclear how the approach to a terminal state plays out dynamically at the level of individual cells. One of the best-studied terminal differentiation processes is sporulation of the bacterium *Bacillus subtilis*, through which a vegetative cell under nutritional stress transforms into a stable, dormant spore [46] (see also Fig. 1.1). In some conditions, progression towards the terminal state spans several cell cycles, after which a precise sequence of molecular events remodels the cell into a spore [19, 35, 62]. The number of these pre-sporulation cell cycles can vary even among genetically identical cells in the same microenvironment. Although much of the genetic circuitry regulating sporulation initiation is known, it is still unclear how cells control the different timescales and the sequence of events leading to differentiation.

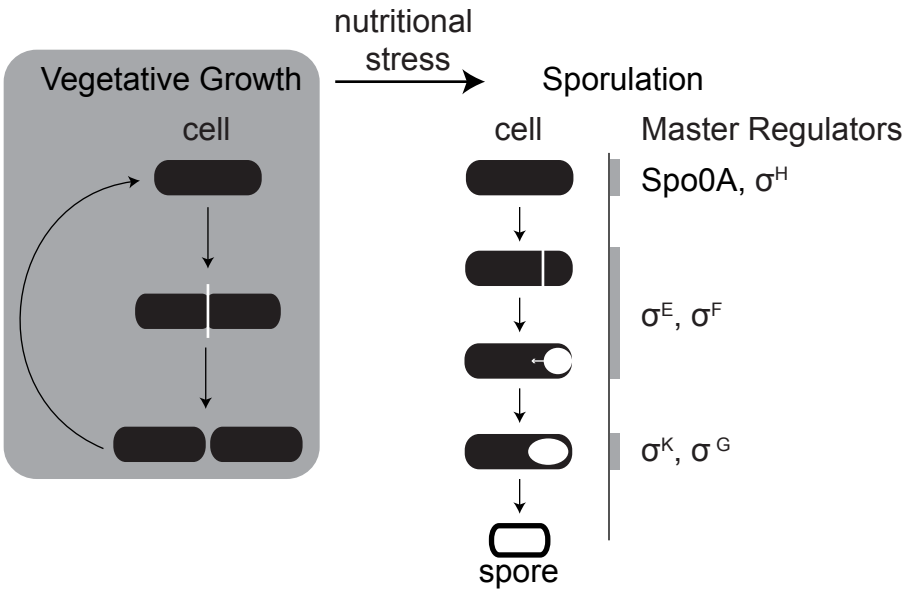

Figure 1.1: A vegetatively growing *B. subtilis* cell divides symmetrically into two daughter cells, each of which is capable of further growth and division. Under nutritional stress, such a cell can cease growth and transform into a stable, dormant spore. After the initiation of sporulation, the cell divides asymmetrically into two cells of different sizes. While both cells are required for spore formation, they have different fates. The smaller cell develops into the spore, whereas the larger cell engulfs the smaller cell, aids its development, and eventually lyses. This series of morphological changes is coupled to distinct programs of gene expression, orchestrated by a set of master regulators.

Progression to sporulation is regulated by a phosphorelay signaling circuit em-

bedded in transcriptional feedback loops. *B. subtilis* cells control sporulation by modulating the phosphorylation and expression of the master transcription factor Spo0A. The phosphorylation of Spo0A is controlled by a four-component phosphorelay, while its expression is controlled by Spo0A itself, as well as other regulators, some of which are also under the direct or indirect control of Spo0A (Fig. 1.2) [12, 43–45]. The inputs to this signaling circuit are five sporulation kinases, KinA–KinE (for simplicity, only KinA is shown in the figure), which autophosphorylate in response to nutrient limitation and other stresses, allowing them to transfer phosphates to Spo0F, which are then reversibly relayed via Spo0B to the master regulator Spo0A [12]. Additionally, Spo0F and Spo0A are dephosphorylated by the Rap and Spo0E family of phosphatases, respectively [43–45]. The KinA–KinE kinases can also act as phosphatases for Spo0F [11, 51]. The phosphorylated form of Spo0A, denoted Spo0A∼P, controls the expression of *kinA*, *spo0F*, and *spo0A* itself (but not *spo0B*) (Fig. 1.2), forming several feedback loops, which could be critical for the all-or-none nature of sporulation initiation [61].

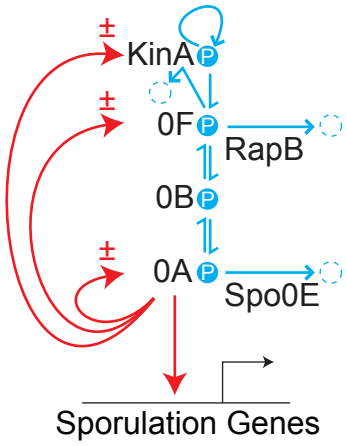

Figure 1.2: Diagram of the sporulation initiation circuit in *B. subtilis*. The main phosphorelay is embedded inside multiple transcriptional feedback loops (red arrows). Kinase autophosphorylation, phosphotransfers, and phosphatase activities are shown in blue arrows. RapB and Spo0E are examples of phosphatases that remove phosphate from the indicated proteins.

The feedback loops in this sporulation circuit have three striking features: First, the activities of the promoters controlling *spo0A*, *spo0F*, and *kinA* (referred to as P_{0A}, P_{0F}, and P_{kinA} in what follows) respond in a "bandpass" manner to varying concentrations of

Spo0A∼P. That is, they are activated by low levels of Spo0A∼P, and repressed by high levels of Spo0A∼P [24], similar to the type of regulation shown to occur in the P_{RM} promoter of phage lambda in response to CI [47]. Second, as discussed through a model in Chapter 2, there is an additional post-translational "bandpass" regulatory effect due to the dual role of Spo0F, which is required for Spo0A phosphorylation but can also lead to Spo0A dephosphorylation, due to reverse phosphotransfer and the activity of Spo0F phosphatases. These effects can cause net phosphorylation of Spo0A to first increase, and then decrease, as Spo0F levels rise [13]. Third, gene expression during progress to sporulation occurs in a pulse-like fashion every cell cycle [35, 62]. In particular, Spo0A's target promoters, including P_{0A} and P_{0F}, pulse once per cell cycle, implying a periodic modulation of the phosphorelay activity, possibly driven by modulation of kinase activity. As a result of these features, models based only on continuous, monotonic interactions between components are inadequate to explain the dynamic behavior of this system.

Phosphorelays are an architectural variant of a canonical two-component signaling system. The genetic circuit described above is a classic example of a signaling circuit. In cells, signaling circuits provide a link between environmental variables, such as light intensity, pheromone levels, and availability of nutrients, and the activities of various transcriptional and post-transcriptional regulators. Signaling circuits exist in many different forms: The simplest circuits consist of enzymes like LacI whose transcriptional activity is modulated by the presence or absence of a bound sugar molecule [60]. Another large category of signaling circuits is based on modulating the activity of a protein by phosphorylation. These include mitogen-activated protein kinase (MAPK) signaling cascades that occur in numerous eukaryotic contexts from yeast to humans [48], and two-component signaling circuits ubiquitous in bacteria [29, 56].

A striking feature of two-component system circuits is that they exist in different architectures (Fig. 1.3). The simplest two-component system architecture has three reactions (Fig. 1.3a,b)— input-dependent autophosphorylation of a sensor kinase, phosphotransfer from the sensor kinase to a response regulator, and dephosphorylation of the response regulator [56]. This phosphotransfer takes place from a unique histidine residue on a domain of the sensor kinase (green block in Fig. 1.3a,b) to a unique aspartate residue on a domain of the response regulator (red block in Fig. 1.3a,b). In many cases, the kinase has

an additional role in dephosphorylating the response regulator, and this bifunctionality can make the response robust to the concentration of the two components via an integral feedback mechanism [7, 51, 54] (Fig. 1.3c). More complex two-component system architectures include a cascade of phosphotransfers across several protein components, such as in the phosphorelay [12] (Fig. 1.3d), which can integrate more inputs than a simple two-component system. Often, two or more components in a phosphorelay exist as separate domains of the same protein component (Fig. 1.3e) [26]. The potential for multiple phosphorylation in these hybrid proteins has been shown to increase the magnitude of response sensitivity [33].

An examination of the phosphorelay architecture and its operation during sporulation progression reveals three striking aspects: First, because it has more components than the simple two-component system architecture, it can integrate more inputs, even if multiple inputs act on the same component. Second, as stated above, it can exhibit a post-translational bandpass effect, which might play a critical role in its operation during sporulation progression. Third, it highlights how different contexts of the phosphotransfer reaction allow the generation of architectural diversity in two-component systems (Fig. 1.3). For example, a cascade of phosphotransfers gives rise to a phosphorelay. On the other hand, coupling phosphotransfer with phosphatase activity of the kinase generates the bifunctional two-component system architecture. Finally, constraining phosphotransfer to be intramolecular rather than intermolecular generates hybrid phosphorelays. These considerations offer opportunities to revisit questions of how cells can potentially utilize the phosphorelay architecture, and, more fundamentally, the phosphotransfer reaction.

1.3 Thesis Overview

In Chapter 2, we examine how pulsed bandpass feedback loops in the phosphorelay circuit operate in individual cells during sporulation progression. For this, we combine mathematical modeling of the phosphorelay circuit with single-cell measurements of key circuit interactions. We note the presence of an additional post-translational layer of bandpass regulation in the model. The model also predicts the appearance of a delayed phase shift in the pulsed activities of circuit components, which we verify experimentally using time-lapse fluorescence microscopy. The dynamical structure of the model contains an alternate cellu-

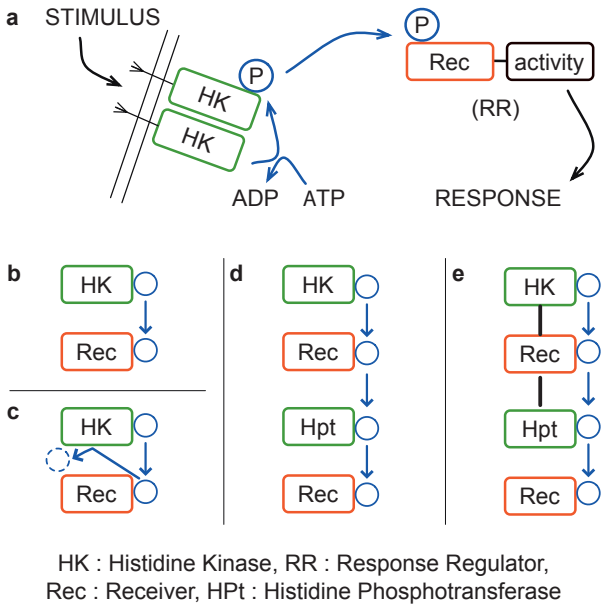

Figure 1.3: Signal transduction in two-component systems. (a) Stimulus levels are transduced into phosphates by a histidine kinase (HK). These phosphates are transferred from the histidine kinase to the receiver domain (Rec) of a response regulator protein. The phosphorylation status of the receiver domain regulates the activity of the response regulator. Red and green borders indicate protein domains where the phosphate is on the histidine and aspartate residues, respectively. (b) Schematic of a simple two-component system showing phosphotransfer from the histidine kinase to the receiver domain of the response regulator. (c) Architectural variant of the two-component system where the histidine kinase has an additional role in dephosphorylating the receiver domain of the response regulator. (d) Phosphorelay architecture where phosphate is transferred from the histidine kinase to the receiver domain of the response regulator via intermediatory phosphotransfer steps: First phosphotransfer is from the histidine kinase to a protein with only a receiver domain, second phosphotransfer is from this receiver domain to the histidine residue of another phosphotransferase protein (Hpt), and third phosphotransfer is from this residue to the receiver domain of the response regulator. (e) Two-component system architecture in which phosphotransfers occur between domains of the same protein. Thick black lines connect domains that exist on the same protein component.

lar state with no phase shift. This feature can be accessed with a circuit perturbation, and is also verified experimentally. These results illustrate the dynamics possible in a genetic circuit with pulsed bandpass feedback loops, and highlight the interplay between timescales of an external periodic input and the circuit components. We have recently submitted these results to the journal *PLoS ONE*.

Chapter 3 examines the architectural significance of the core phosphorelay against the backdrop of the family of two-component systems. Here, we address this issue computationally based on how the phosphorelay circuit structure operates in the physiological context of sporulation. Further, we explore how the phosphotransfer reaction, a basic building block of the phosphorelay and simpler two-component systems, affects the stimulus-response curve. We find that the two phosphorelay phosphatases can serve as tuning parameters to adjust the two thresholds of the post-translational bandpass response. We also find that the phosphotransfer reaction can be used to increase the range of sensitivity of response to stimulus, thereby allowing two-component systems to operate as signaling amplifiers. A similar conclusion to this result, also presented here [53], has been recently reported using a complementary approach [15]. These results emphasize signaling properties of two-component system architectures that may explain their role inside cells, and we discuss how these roles have broad correlations with the design of electrical circuits.

These results on the dynamical implications of the phosphorelay circuit structure and the signaling consequences of its architectural features are summarized in Chapter 4. In this chapter, we also propose theoretical and experimental directions for further investigation: First, we highlight molecular interactions and methods to identify their mechanisms that might be crucial to understand the dependence of sporulation initiation on circuit dynamics. Second, we suggest how the observed temporal patterns might assist mechanical processes immediately after initiation of sporulation. Third, we propose using the universal engineering constraint of power consumption to understand the role of architectural diversity in two-component systems. These directions have the potential to deepen our understanding of the relationship between phosphorelay dynamics and sporulation initiation, and transfer insights from engineering design to genetic circuits.

In this thesis, we make several primary contributions. First, we characterize, at the single-cell level, key bandpass input-output interactions in a phosphorelay circuit underlying a canonical terminal differentiation process. Second, we develop a simple mathematical

model based on these measurements, and analyze its operation under conditions prevailing in real cells. The model predicts the emergence of a delayed phase shift between circuit components, whose existence we verify experimentally using time-lapse fluorescence microscopy. Third, we predict an alternate cellular state in the model that can be accessed using a perturbation to the circuit, and show that similar behavior can be observed experimentally. Fourth, we explore the architectural potential of the core phosphorelay in the context of the superfamily of two-component system architectures, showing that two types of phosphorelay phosphatases enable independent tuning of a post-translational bandpass response, and that phosphorelay building blocks can be used to construct linear signaling amplifiers.

Chapter 2

Dynamical Implications of Phosphorelay Circuit Structure

In this chapter, we ask how the bandpass and pulsatile features of the phosphorelay circuit affect the approach to sporulation in individual cells. We address this question through a combination of mathematical modeling and single-cell monitoring via time-lapse fluorescence microscopy. Our data show that the bandpass input functions of P_{0A} and P_{0F} are shifted relative to each other. A simple mathematical model incorporating these constraints (transcriptional bandpasses plus discrete pulses in kinase activity) predicts the additional post-translational bandpass regulation of Spo0A∼P activity by Spo0F expression level. The model also predicts the appearance of a delayed phase shift between pulses of P_{0A} and P_{0F} activity, after they have been in phase for several cell cycles. Our experiments verified the existence of this delayed phase shift. Further analysis of the model indicates the possibility of an additional state in which no phase shift appears between these promoter activity pulses. Consistent with this prediction, strains containing extra copies of *spo0F* showed additional steady-state-like behavior with no phase shift between P_{0A} and P_{0F} pulses. Together these results provide insight into the interplay between the periodic input to the sporulation circuit and the dynamics of its components.

2.1 Transcriptional Bandpasses

In order to characterize the feedback dynamics of the sporulation circuit, we first investigated the quantitative dependence of the activity of the *spo0A* and *spo0F* promoters, denoted P_{0A} and P_{0F}, respectively, on Spo0A∼P levels. To do so, we took advantage of

the Spo0A^{sad67} allele, which is known to transcriptionally regulate target promoters without the need for phosphorylation [23, 31]. We constructed two strains (Fig. 2.1a) in which Spo0A^{sad67} controlled expression of the yellow fluorescent protein, YFP, from either the P_{0A} or the P_{0F} promoter. In both strains, Spo0A^{sad67} was expressed from the IPTG-dependent $P_{hyperspank}$ inducible promoter, denoted P_{hyp} [23]. These strains also incorporated a second copy of P_{hyp} driving expression of cyan fluorescent protein, CFP, for calibration.

At the start of the experiment, each of the two strains was induced with the same amount of IPTG, and imaged over time using time-lapse microscopy (Fig. 2.1b). As Spo0A^{sad67} expression levels increased towards their steady state value, we quantified the activity of the downstream promoters, determined by the rate of increase in YFP fluorescence (see Appendix B), as well as the mean fluorescence of the calibration reporter (Fig. 2.2a,b) [17, 19, 37, 58, 59]. Then, we plotted these P_{0A} and P_{0F} promoter activities against the level of the calibration reporter (and thus of Spo0A^{sad67}) from the same cell (Fig. 2.2c,d). For both promoter reporters, these measurements were performed on cells growing in similar microenvironments and fluorescent illumination conditions.

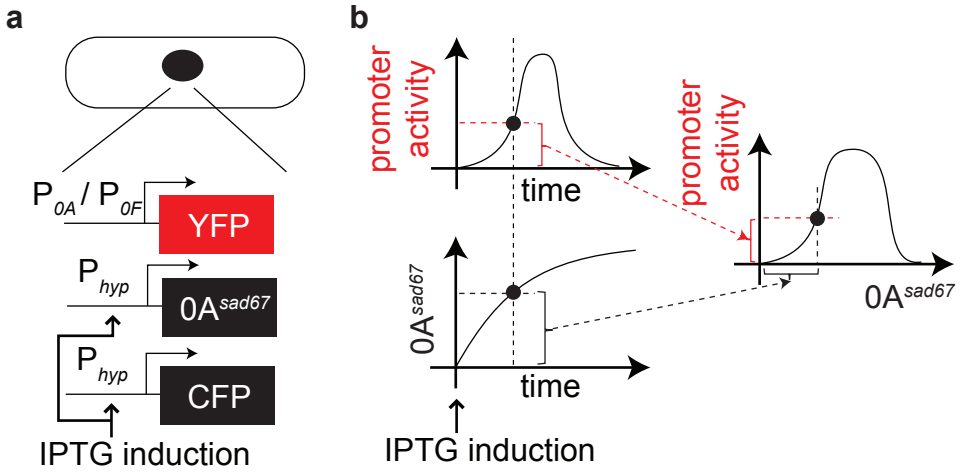

Figure 2.1: (a) Schematic of the strains and (b) the method used to measure the bandpass functions of P_{0A} and P_{0F}.

The data provided a quantitative measurement of the bandpass input functions for P_{0A} and P_{0F} (Fig. 2.2c,d and Fig. 2.3). Despite variability, we found that the two promoter reporters displayed both broadly similar features and systematic differences. Thus, although they exhibited coincident pulses of activity, P_{0A} exhibited greater basal fluorescence ex-

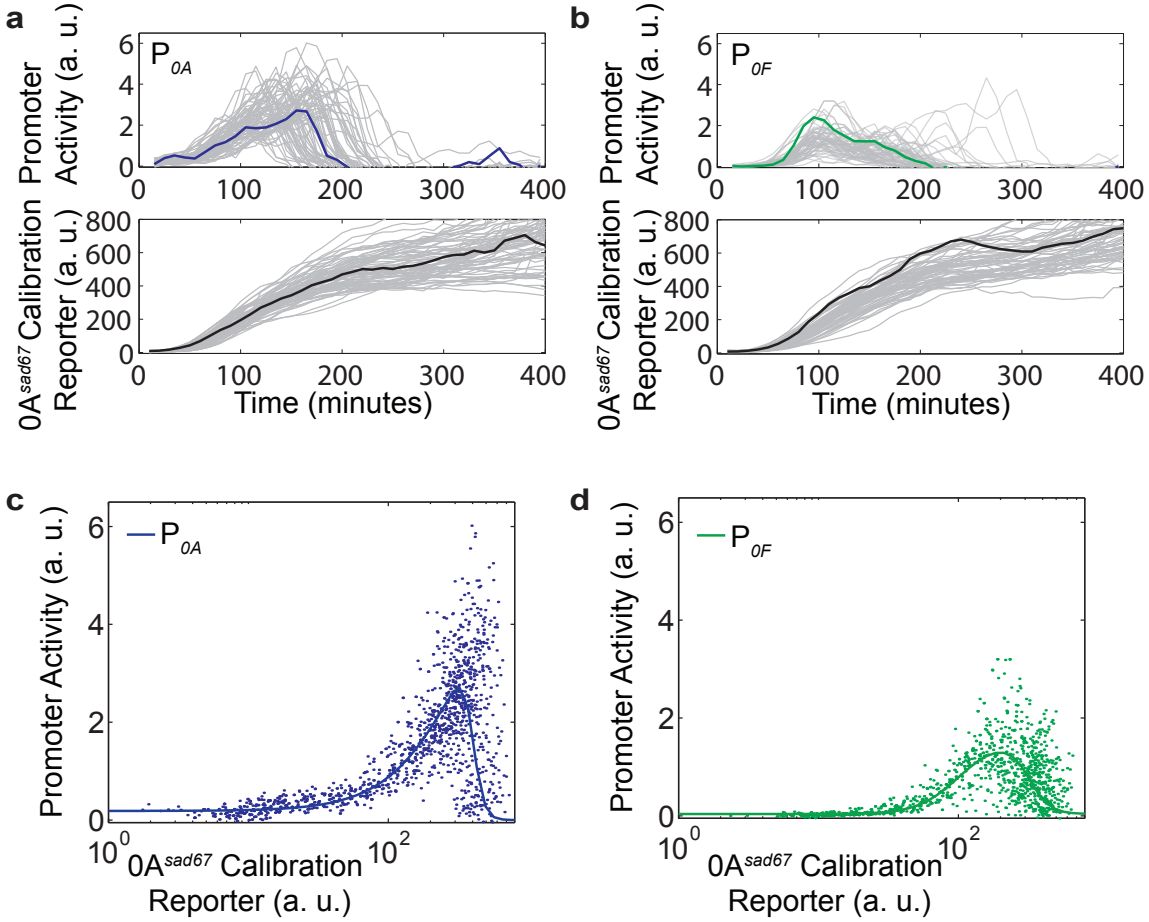

Figure 2.2: Transcriptional bandpasses in the sporulation initiation circuit. (a)–(b) Single-cell measurements of promoter activities of P_{0A} ($N = 75$) and P_{0F} ($N = 64$) (top panels), and corresponding induction profiles of the Spo0A^{sad67} calibration reporter (bottom panels). Individual traces are shown in gray. A specific trace in each plot is highlighted in color line. (c)–(d) Single-cell measurements represented as P_{0A} /P_{0F} promoter activity versus the Spo0A^{sad67} calibration reporter (dots). Solid lines show a fit resulting from the following set of parameter values: $n_A = 1.6$, $m_A = 12$, $n_F = 3$, $m_F = 6$, $K_F = 100 a.u.$, $K_A = 3.5K_F$, $J_A = 4K_F$, $J_F = 3.2K_F$, $\alpha_{0A} = .4K_F$, $\alpha_{0F} = 0.025$, $\beta_{0A} = 6 a.u.$, $\beta_{0F} = 1.5 a.u.$.

pression at low Spo0A^{sad67} levels, a higher total fluorescence expression level, and a sharper shutoff at high Spo0A^{sad67} levels, compared to P_{0F}.

To gain insight into the origins of the observed variability, we compared the difference between a cell and its sister cell with the difference between the same cell and a randomly chosen surrogate sister cell (Appendix Fig. B.1). Here, the difference metric for two given traces is the cumulative sum in time of the absolute difference between them. The difference between sister cells was significantly smaller than that between surrogate sister cells (Appendix Fig. B.1), suggesting that variable features can be inherited between cell generations.

In order to incorporate the measured bandpass functions into a model of the phosphorelay circuit, we modeled the experimental data using standard promoter activity rate functions that incorporate both activation and repression (solid lines, Fig. 2.2c,d):

$$P_{0A} = \beta_{0A} \frac{\alpha_{0A}^{n_A} + x^{n_A}}{K_A^{n_A} + x^{n_A}} \frac{J_A^{m_A}}{J_A^{m_A} + x^{m_A}}, \tag{2.1}$$

$$P_{0A} = \beta_{0F} \left(\alpha_{0F} + \frac{x^{n_F}}{K_F^{n_F} + x^{n_F}} \frac{J_F^{m_F}}{J_F^{m_F} + x^{m_F}} \right). \tag{2.2}$$

Here, x represents [Spo0A$\sim$P], while the K_i and J_i parameters represent, respectively, the activation and repression thresholds of the transcriptional bandpasses. A heuristic fit of this model to the data is shown in Fig. 2.2c,d and in Fig. 2.3.

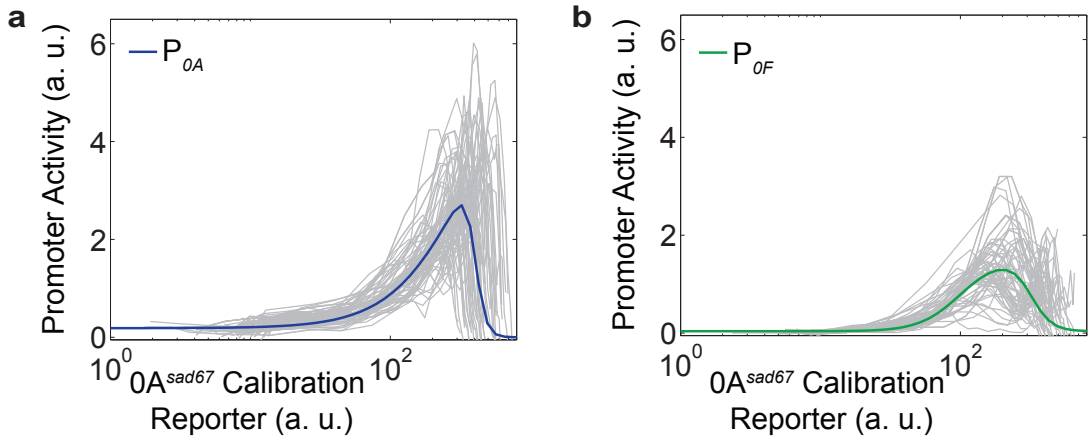

Figure 2.3: Transcriptional bandpasses in the sporulation initiation circuit. (a)–(b) Single-cell measurements represented as P_{0A} /P_{0F} promoter activity versus the Spo0A^{sad67} calibration reporter. Individual traces are shown in gray. Green and blue lines are the heuristic fits from Fig. 2.2c,d.

Together, these results show that P_{0A} and P_{0F} encode similarly shaped bandpass functions, but with systematic differences in their quantitative parameters.

2.2 Post-Translational Bandpass

Next, we constructed a simple mathematical model of the phosphorelay based on its phosphorylation, dephosphorylation, and phosphotransfer reactions. These reactions are modeled using ordinary differential equations based on standard mass action kinetics. The model consists of four equations representing the phosphorylated forms of the phosphorelay proteins KinA (K_p), Spo0F (F_p), Spo0B (B_p), and Spo0A (A_p),

$$\begin{aligned}
\frac{dK_p}{dt} &= k_s(K_T - K_p) - k_t K_p(F_T - F_p), \\
\frac{dF_p}{dt} &= k_t K_p(F_T - F_p) - k_t F_p(B_T - B_p) + k_{-t} B_p(F_T - F_p) - k_h(K_T - K_p)F_p - k_r F_p, \\
\frac{dB_p}{dt} &= k_t F_p(B_T - B_p) - k_{-t} B_p(F_T - F_p) - k_t B_p(A_T - A_p) + k_{-t} A_p(B_T - B_p), \\
\frac{dA_p}{dt} &= k_t B_p(A_T - A_p) - k_{-t} A_p(B_T - B_p) - k_e A_p.
\end{aligned}$$

Here, K_T, F_T, B_T, and A_T represent total levels of the phosphorelay proteins, $k_{\pm t}$ is the rate of forward/backward phosphotransfer rates in the phosphorelay, k_s is the rate of autophosphorylation of the kinase, k_e and k_r are the dephosphorylation rates of Spo0A and Spo0F by their phosphatases, respectively, and k_h is the rate of dephosphorylation of Spo0F by KinA. The parameter values used for this set of equations are listed in Table 2.1. The choice of these parameter values was guided by the notion that reactions mediating phosphate flux are typically faster than the cell-cycle timescale ($\sim 1/hr$). The rate constants for the bimolecular reactions in the model (see Table 2.1) are similar to effective rate constants for the phosphotransfer reactions estimated from *in vitro* experiments [28].

Using this model, we first computed the response of A_p to different Spo0F expression levels and observed a bandpass response (Fig. 2.4). Removal of reverse phosphotransfer from the model ($k_{-t} = 0$) completely abolishes the inhibition of A_p by high Spo0F levels (Appendix Fig. C.1a,c), showing that reverse phosphotransfer is necessary for this bandpass response. Similarly, when the Spo0F phosphatase activity is set to zero in the model ($k_r = k_h = 0$), high levels of Spo0F do not inhibit A_p (Appendix Fig. C.1b,c). This bandpass response is also seen in a more realistic model of the phosphorelay circuit that

Parameter	Value
K_T	$1000nM$
B_T	$1000nM$
A_T	$1000nM$
$k_{\pm t}$	$1/(nM \cdot hr)$
k_s	$100/hr$
k_r	$100/hr$
k_e	$100/hr$
k_h	$1/(nM \cdot hr)$

Table 2.1: Parameters for the phosphorylation, phosphotransfer, and dephosphorylation reactions of the phosphorelay circuit model.

includes cell-cycle-dependent pulsing and transcriptional feedbacks (Appendix Fig. C.2a–c), as well as in a more complicated reaction scheme of the core phosphorelay (Appendix C, Appendix Fig. C.2d). Thus, the bandpass response of Spo0A phosphorylation to Spo0F levels in this model is a direct result of reversibility of the phosphotransfer, which allows phosphates to flow backwards from Spo0A to Spo0F, where they can be hydrolyzed by Spo0F phosphatases and lost from the system.

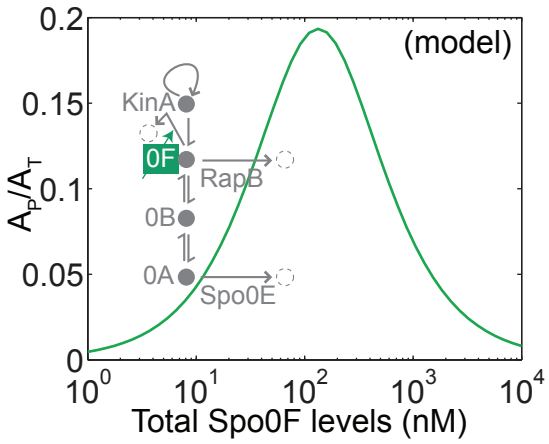

Figure 2.4: Phosphorelay activity depends on total Spo0F levels in a bandpass manner. Fraction of phosphorylated Spo0A computed for different Spo0F levels in the phosphorelay model.

Experiments confirm the post-translational bandpass of phosphorelay activity. The prediction that Spo0F levels have a bandpass effect on Spo0A activity is in qualitative agreement with previous experimental results [13]. To measure the post-translational bandpass at the level of single cells, we induced Spo0F to different levels using a Spo0F-CFP protein under the IPTG-controlled promoter P_{hyp} in a strain where the endogenous

copy of *spo0F* was deleted (Fig. 2.5). We quantified the resulting activity of Spo0A∼P activity by measuring the peak amplitude of the P_{0F}-YFP pulses. We observed a striking bandpass response similar to that predicted by the model (Fig. 2.6). The physiological response of sporulation was inhibited at the highest IPTG induction (results not shown), indicating that the bandpass response is due to low Spo0A∼P and not an artifact of the transcriptional bandpass in the P_{0F} reporter.

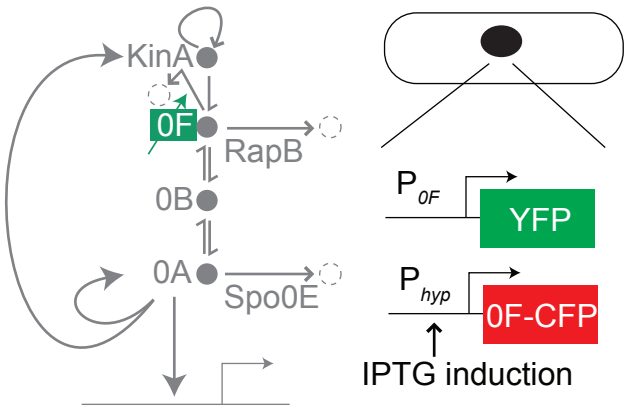

Figure 2.5: Diagram of the sporulation circuit and the strain schematic used to test the post-translational bandpass prediction (compare to Fig. 1.2).

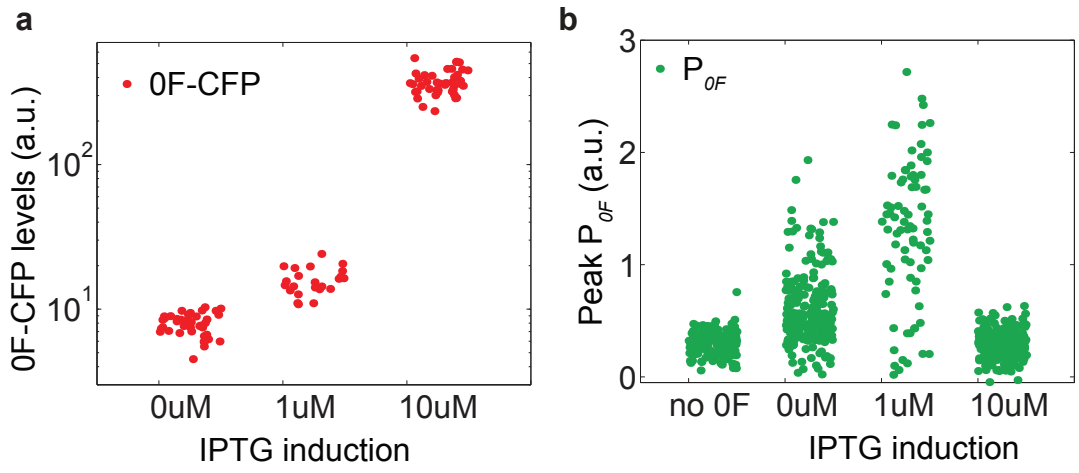

Figure 2.6: Measurement of the Spo0F post-translational bandpass. (a) As the amount of inducer IPTG is increased (0uM, 1uM, 10uM), there is an increase in Spo0F induction level. (b) Peak P_{0F} pulse amplitude over time for different IPTG induction levels has a bandpass shape. There is some activity even at 0uM IPTG possibly due to basal expression of Spo0F, although it is too low to induce sporulation.

2.3 Delayed Phase Shift

Next, we incorporated the cell-cycle-dependent pulsatile regulation of phosphorelay activity into the model. For simplicity, we assumed that the kinase autophosphorylation rate is a square wave ($k_s(ON/OFF)$), with a period fixed at 3 hours, similar to the cell-cycle times observed experimentally (Fig. 2.7). We further assumed, arbitrarily, that the duration of the "ON" phase spanned 50% of that period. We also included in the model the feedbacks on the phosphorelay proteins based on the transcriptional bandpass measurements. In this more complete model, the total level of each phosphorelay protein can increase due to transcription and decrease by degradation. While both phosphoforms can be degraded, we assume that transcription creates only unphosphorylated proteins. These reactions are also modeled using ordinary differential equations. Because there are no known active degradation processes for these proteins, we assume that the only source of degradation is dilution by cell growth, which is modeled as a first-order decay process with rate constant γ. With these assumptions, we obtain the following equations for the total concentrations of the phosphorelay proteins KinA, Spo0F, Spo0B, and Spo0A, denoted K_T, F_T, B_T, and A_T, respectively:

$$\begin{aligned}
\frac{dK_T}{dt} &= P_{kinA}(A_p) - \gamma K_T, \\
\frac{dF_T}{dt} &= P_{0F}(A_p) - \gamma F_T, \\
\frac{dB_T}{dt} &= P_{0B} - \gamma B_T, \\
\frac{dA_T}{dt} &= P_{0A}(A_p) - \gamma A_T.
\end{aligned}$$

Here we assume that protein degradation is negligible compared to protein dilution. Hence, $\gamma = 1/hr$, similar to the rates of dilution by cell growth observed experimentally. This degradation term is also added to the equations of the phosphorylated proteins. The mean rates of expression from the P_{0F} and P_{0A} promoters, as functions of Spo0A$\sim$P(A_p), are denoted $P_{0F}(A_p)$ and $P_{0A}(A_p)$, respectively, and are based on the empirically determined bandpass functions, given by Eqs.(2.1)–(2.2). The bandpass parameters are constrained by the experimental measurements above, with the free parameter K_F chosen to be $K_F = 100nM$, similar to values of Spo0A$\sim$P's DNA binding affinity estimated from previous experiments [22]. Additionally, because previous results suggest that the promoter of KinA is also a band-

pass like that of Spo0A [24], we assume that $P_{kinA}(A_p) = P_{0A}(A_p)$ (the importance of this assumption is checked in the dynamical analysis described below). There is no known transcriptional regulation of Spo0B by Spo0A∼P. Moreover, experimental measurements show that expression level of a fluorescent reporter fused to P_{0B} is already turned on prior to the beginning of progression to sporulation, and that this reporter changes less than twofold during sporulation initiation (Appendix Fig. B.2). Consequently, we assume P_{0B} to be constant, $P_{0B} = \beta_{0B}$. The maximal expression strengths of these promoters are free parameters and are set to $\beta_{0A} = 15000nM/hr$, $\beta_{0B} = 6000nM/hr$, $\beta_{0F} = 2280nM/hr$. The parameters used in this set of equations are summarized in Table 2.2.

Parameter	Value
$k_s(ON)$	$100/hr$
$k_s(OFF)$	$1/hr$
γ	$1/hr$
n_A	1.6
m_A	12
n_F	3
m_F	6
K_F	$100nM$
K_A	$3.5K_F$
J_A	$4K_F$
J_F	$3.2K_F$
α_{0A}	$0.4K_F$
α_{0F}	0.025
β_{0A}	$15000nM/hr$
β_{0F}	$2280nM/hr$
β_{0B}	$6000nM/hr$

Table 2.2: Parameters for the periodic input and the production-degradation reactions of the phosphorelay circuit.

In order to understand the implications of the bandpass regulation on the dynamics of the phosphorelay in cells, we first set out to simplify the model by reducing its dimensionality. The model has eight dimensions: expression levels of the four proteins and their phosphorylation states. However, because the timescale of phosphorylation is much faster than that of protein production and degradation, the four degrees of freedom corresponding to phosphorylation can be adiabatically eliminated. In addition, since P_{0B} is constant, B_T can be set to a fixed value. Third, having assumed $P_{kinA} = P_{0A}$, KinA and Spo0A protein levels are represented by the same degree of freedom. These considerations allow

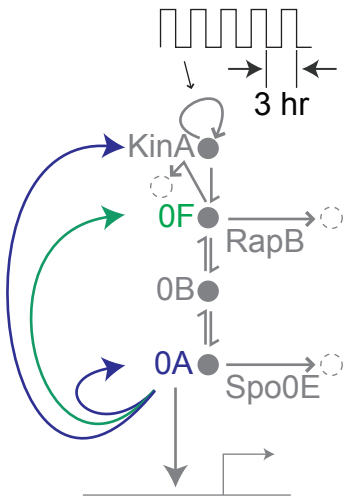

Figure 2.7: Diagram of the phosphorelay circuit driven by square wave pulses in kinase autophosphorylation.

us to reduce the model to two effective dimensions, one for total Spo0A and another one for Spo0F:

$$\begin{aligned} \frac{dF_T}{dt} &= P_{0F}(A_p) - \gamma F_T, \\ \frac{dA_T}{dt} &= P_{0A}(A_p) - \gamma A_T. \end{aligned}$$

In this reduced model, the promoter activities P_{0A} and P_{0F} are functions of A_p, which itself is a function of the values of the total levels of the phosphorelay proteins and the input square wave. This dependence is computed from the equations of the phosphorylated proteins (see Appendix C).

To analyze the dynamic behavior of this two-dimensional model, we computed the nullclines $\frac{dF_T}{dt} = 0$ and $\frac{dA_T}{dt} = 0$ on the Spo0A-Spo0F phase plane. The trajectories in the two-dimensional model switch between two phase planes, corresponding to the "ON" and "OFF" parts of the square wave (Fig. 2.8). For the parameters chosen, the nullclines cross at a single point in both phase planes, which is a stable steady state. Consider the trajectory starting near the origin, where levels of phosphorelay proteins are low (gray and red lines in Fig. 2.8). Such a trajectory spends the first few periods traversing up and down a single line passing through the origin, for which Spo0A and Spo0F are proportional to (i.e., in phase with) each other, and then curves away from this line (see Fig. 2.8). At that point

the proportionality between Spo0A and Spo0F breaks down, leading to the appearance of a phase shift between the activities of the P_{0A} and P_{0F} promoters (Fig. 2.9). The assumption that $P_{kinA}(A_p) = P_{0A}(A_p)$ does not qualitatively change the dynamical picture described here (Appendix Fig. C.3).

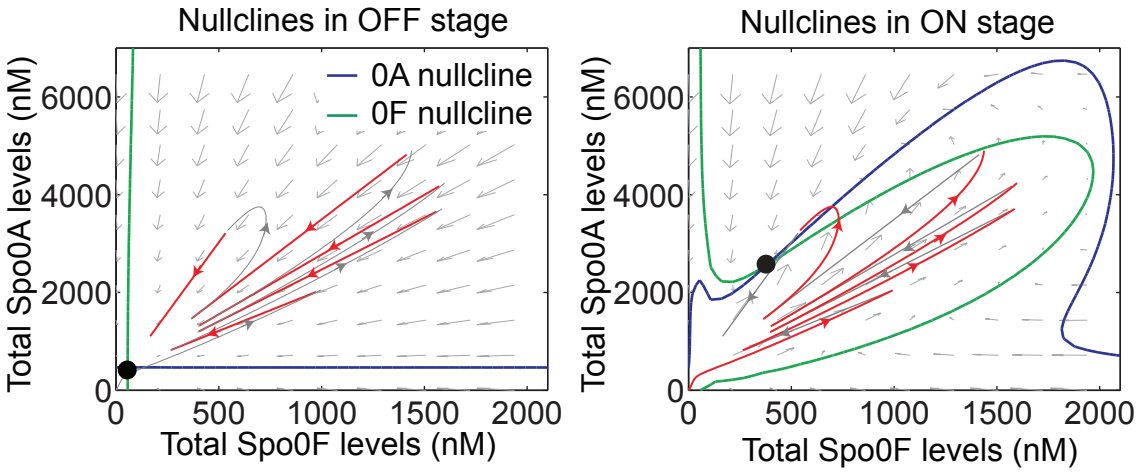

Figure 2.8: Phase portraits computed from the reduced model for "ON" and "OFF" parts of the square wave: Solid lines represent nullclines of Spo0A (blue) and Spo0F (green), arrows depict the slope field, and black circles denote stable steady states. A red-gray color code is used to plot the trajectory on each phase plane, with red marking the portion of the trajectory that evolves on the active phase plane, and gray marking the portion on the other phase plane.

The emergence of this delayed phase shift from the model can be understood in terms of the effect on the transcriptional bandpass functions of P_{0A} and P_{0F} (Fig. 2.10). In the initial periods of the square wave, the peak amplitude of Spo0A∼P pulse is low and it accesses only the activating parts of the promoter input functions. Consequently, the pulses in P_{0A} and P_{0F} are proportional to each other. In the last period, the peak amplitude of Spo0A∼P is higher and it sweeps across the bandpass region. When this happens, there is a time interval in which P_{0F} is repressed while P_{0A} is activated, generating a phase shift between the P_{0A} and P_{0F} pulses. The duration of this phase shift is determined by the rate of increase in Spo0A∼P level, with a faster rate of increase resulting in a smaller duration. In the limit that Spo0A∼P levels reach their final value instantaneously, there is no phase shift.

Delayed phase shift between P_{0A} and P_{0F} can be observed experimentally. To verify experimentally the existence of this delayed phase shift between the activities of

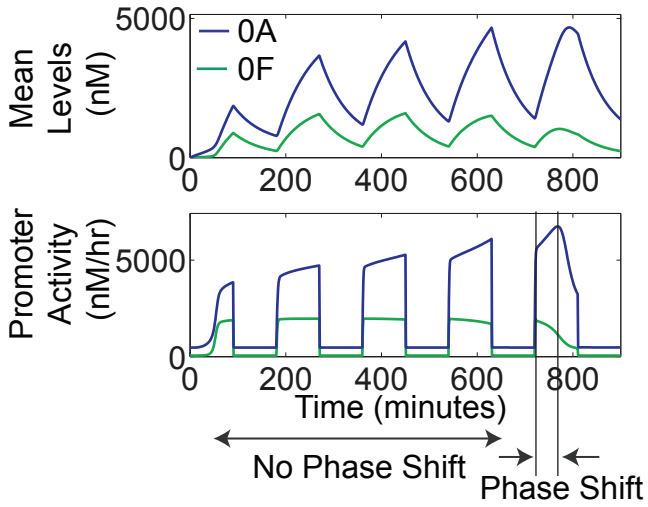

Figure 2.9: Delayed phase shift emerges in the periodic activity of genes P_{0A} and P_{0F} in the phosphorelay circuit. Mean levels of Spo0A and Spo0F (top panel) computed from the complete model, and their corresponding promoter activities (bottom panel).

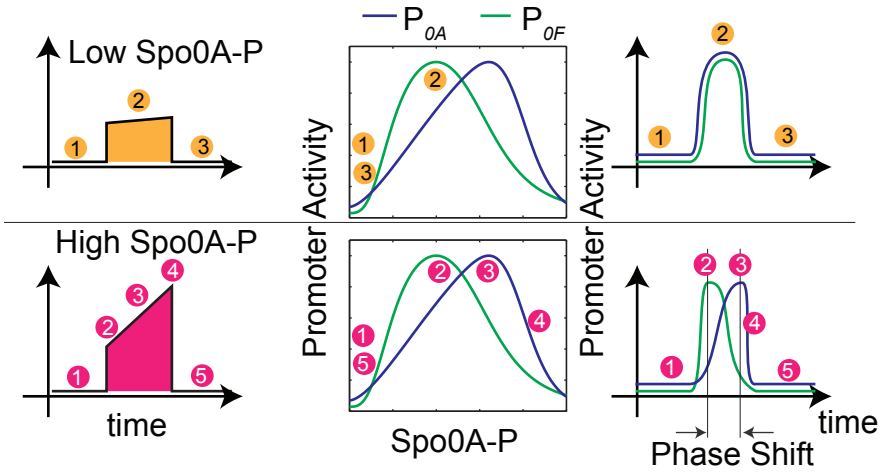

Figure 2.10: Illustration of the delayed phase shift as a mapping from a Spo0A∼P pulse to the transcriptional bandpasses, and from these bandpasses to the promoter activity pulses. Orange circles (top row, 1-2-3) label time-points before, during, and after a low amplitude Spo0A∼P pulse. Pink circles (bottom row, 1-2-3-4-5) label time-points before, during, and after a high amplitude Spo0A∼P pulse. Colored circles are placed at corresponding points on the transcriptional bandpasses and promoter activity pulses.

P_{0A} and P_{0F}, we constructed a two-color strain by which the two promoter activities could be simultaneously measured in the same cell (Fig. 2.11a). Both P_{0A} and P_{0F} pulsed in the sporulation cycles as well as in the pre-sporulation growth cycles (Fig. 2.11b). We found that the distribution of delays between P_{0A} and P_{0F} pulse peaks in the pre-sporulation growth cycles (Fig. 2.11c) is close to zero (1 ± 16 min, $N = 56$), i.e., the promoters pulse in phase, while those in the sporulation cycle are significantly larger than 0 (29 ± 26 min, $N = 83$; KS test, $p < 10^{-7}$).

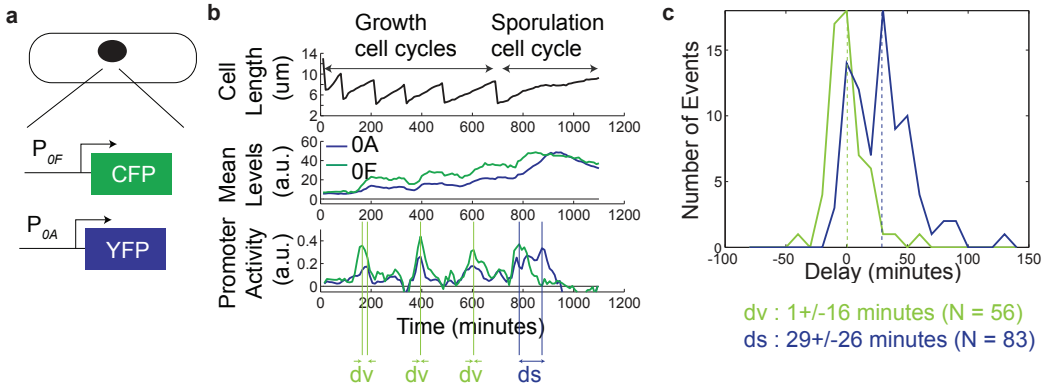

Figure 2.11: Delayed phase shift between P_{0A} and P_{0F} can be observed experimentally. (a) Schematic of the two-color strain used to experimentally measure the single-cell dynamics of P_{0A} and P_{0F}, which are fused to YFP and CFP fluorescent reporters, respectively. (b) Single-cell measurements of P_{0A} and P_{0F} promoter activities (bottom panel), mean levels of YFP and CFP (middle panel), and the cell length (top panel). "dv" and "ds" denote the time difference between the P_{0A} and P_{0F} peak pulse amplitudes in the pre-sporulation vegetative growth cycles and in the sporulation cycle, respectively. (c) Experimentally measured distribution of the P_{0A}-P_{0F} time differences in pre-sporulation vegetative growth cycles and in sporulation cycles.

2.4 Alternate Cellular State

Nullcline analysis of the simplified two-dimensional model is also useful in connecting the delayed phase shift in the phosphorelay dynamics with the post-translational bandpass (Fig. 2.4). In the "ON" phase plane, an increase in *spo0F* copy number (Fig. 2.12) shifts the Spo0F nullcline to the right, which leads to a low A_p fixed point (Fig. 2.13). In this situation, pulses of KinA activity lead to trajectories in phase space for which Spo0A and Spo0F are proportional for the duration of the square wave input. The promoter activities P_{0A} and P_{0F} also maintain their proportionality, and so exhibit no phase shift (Fig. 2.14).

Thus, the model predicts that an increase in *spo0F* copy number should lead to an alternate behavior with low levels of Spo0A∼P, where P_{0A} and P_{0F} pulse permanently in phase with each other.

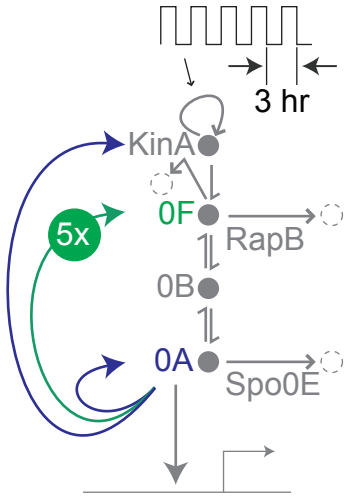

Figure 2.12: Diagram of the phosphorelay circuit with increased *spo0F* copy number.

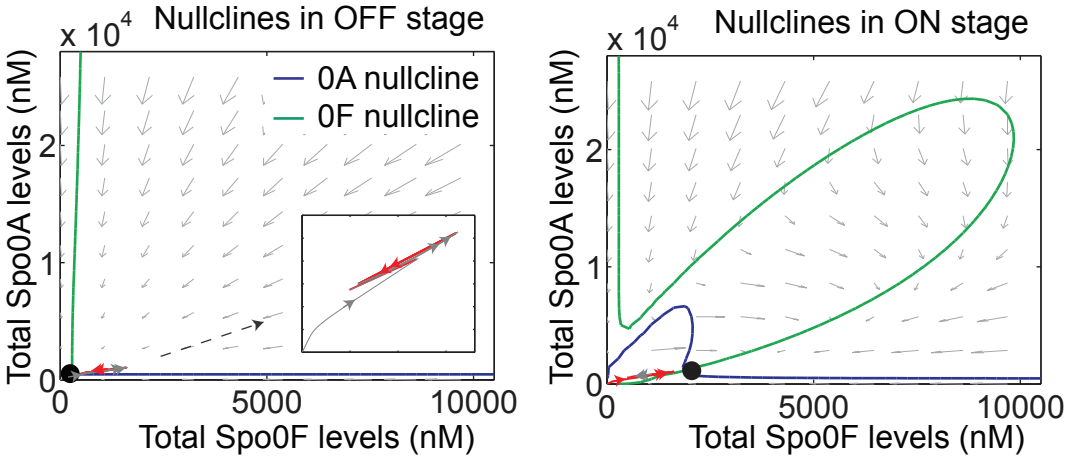

Figure 2.13: Phase portraits computed from the reduced model with increased *spo0F* copy number for the "ON" and "OFF" parts of the square wave.

In terms of the representation in Fig. 2.10, this perturbation in *spo0F* copy number restricts Spo0A∼P activity to low amplitude pulses. Since low amplitude Spo0A∼P pulses can give rise to pulses in P_{0A} and P_{0F}, this perturbed trajectory is similar to the initial periods of the square wave where P_{0A} and P_{0F} pulses are in phase (Fig. 2.9). However, these initial periods are limited in number, whereas in the perturbed system, the phase shift

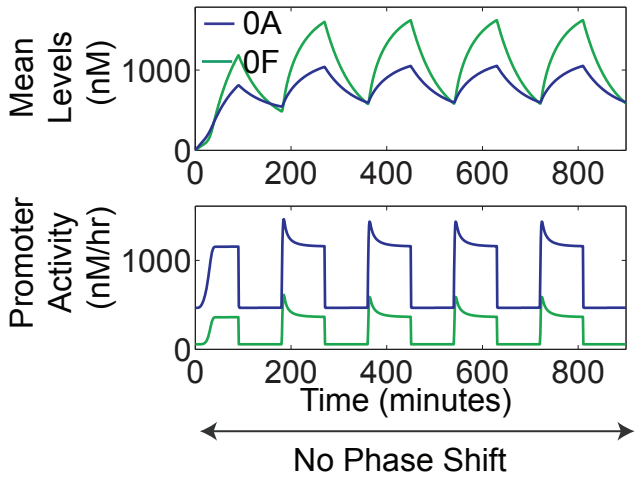

Figure 2.14: No phase shift in perturbed model. Mean levels of Spo0A and Spo0F (top panel) computed from the complete model, and their corresponding promoter activities P_{0A} and P_{0F} (bottom panel).

never appears (Fig. 2.14).

To investigate the dependence of the alternate state on the two types of bandpasses in the model, we examined the changes to the nullclines in response to individual bandpass perturbations. In the absence of reverse phosphotransfer, a feature needed for the post-translational bandpass, there is no alternate state, but the nullclines are strongly perturbed and change their orientation (Appendix Fig. C.4a,b). When the activation and repression parts of the P_{0F} transcriptional bandpass are removed individually, the nullclines are perturbed so that the alternate state exists (Appendix Fig. C.4a,c,d). In comparison to this, when the activation and repression parts of the P_{0A} transcriptional bandpass are removed individually, the nullclines are perturbed but without the appearance of the alternate state (Appendix Fig. C.4a,e,f). So, to a first approximation, it is the coupling of the post-translational bandpass and the P_{0F} transcriptional bandpass that enables the alternate state. Further analysis will be required to map regions in parameter space where the alternate state behavior exists.

To test the predicted effects of increased *spo0F* copy number, we first cloned the entire *spo0F* gene into pHP13, a plasmid with copy number ~ 5 [58]. We transformed this plasmid into the two-color P_{0A}-P_{0F} reporter strain (Fig. 2.15a), and used it to measure the phase shift between P_{0A} and P_{0F}. The distribution of delays between P_{0A} and P_{0F} pulse peaks (-7 ± 13 minutes, $N = 48$) indicates that their activities are in phase, consistent with the

model (Fig. 2.15c,d). Moreover, an additional, indirect line of evidence suggests that cells are in a state resembling the low Spo0A∼P alternate state. The level of Spo0A∼P in these cells is not high enough to initiate sporulation (Fig. 2.15b), but is high enough to elicit pulses in P_{0A} and P_{0F} promoter activities (Fig. 2.15d). Thus Spo0A∼P levels are low, but non-zero. Together, these experimental data qualitatively support the model prediction of an alternate state with higher Spo0F copy number.

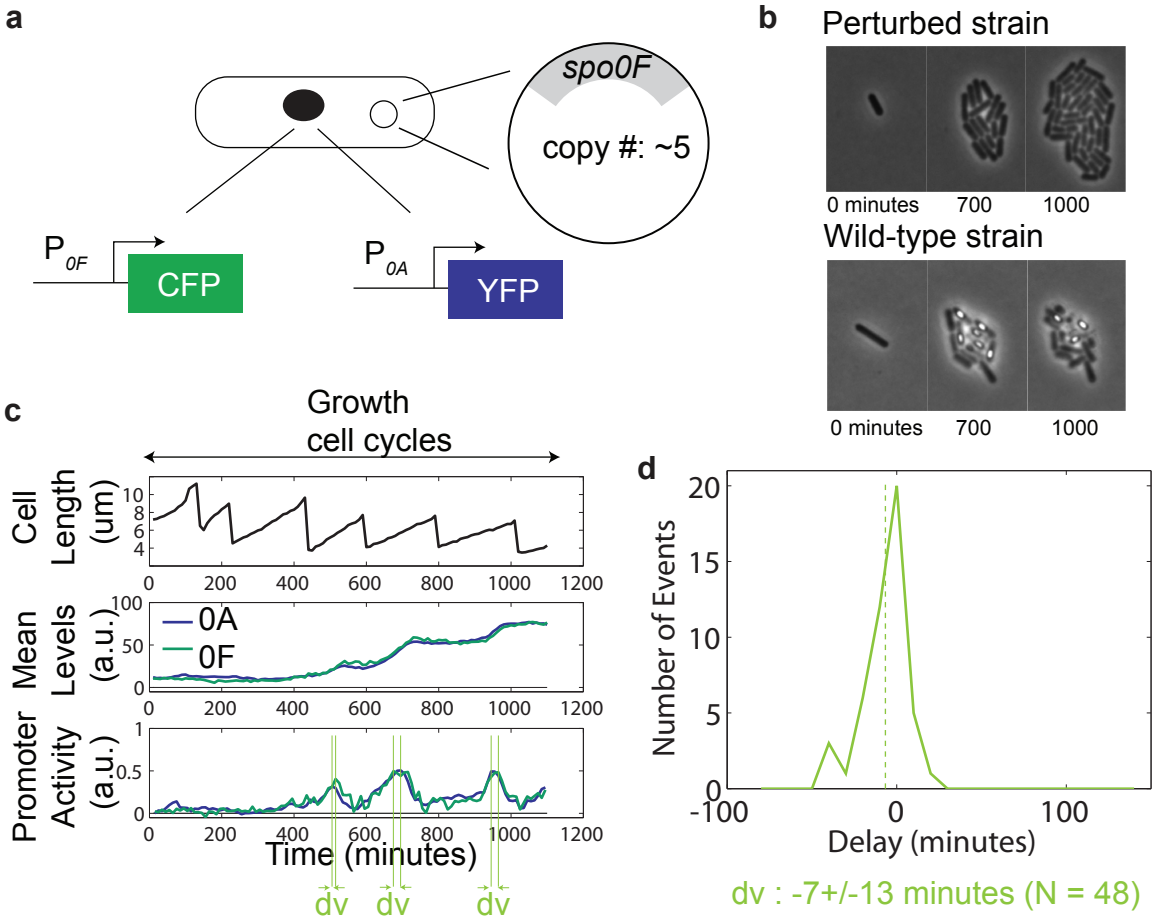

Figure 2.15: Increase in Spo0F copy number leads to a non-sporulating alternate state in which there is no phase shift. (a) Schematic of the strain used to experimentally test the alternate state prediction. (b) Frames from time-lapse movies showing that sporulation in the perturbed strain is inhibited in comparison to the wild-type strain. (c) Single-cell measurements of P_{0A} and P_{0F} promoter activities (bottom panel), mean levels of YFP and CFP (middle panel) and the cell length (top panel). "dv" denotes the time difference between the P_{0A} and P_{0F} peak pulse amplitudes in the pre-sporulation vegetative growth cycles. (d) Experimentally measured distribution of the P_{0A}-P_{0F} time differences in pre-sporulation vegetative growth cycles.

2.5 Interplay between Periodic Input and Circuit Dynamics

The central element of the sporulation circuit in *B. subtilis* is a phosphorelay embedded in bandpass transcriptional feedback loops, which are activated in a pulse-like manner, once per cell cycle. We have investigated the dynamical consequences of this particular architecture through a combination of single-cell monitoring and mathematical modeling. Our mathematical model reveals several striking features of this system, all of which are confirmed experimentally at the single-cell level: First, the response of Spo0A∼P activity has a bandpass dependence on Spo0F protein concentration. Second, pulses in the Spo0A and Spo0F promoter activities are in phase within the initial cell cycles subsequent to stress, but eventually develop a phase shift. Third, an alternate cellular state can be accessed, in which P_{0A} and P_{0F} pulse and remain in phase indefinitely, signifying the presence of low amplitude Spo0A∼P pulses. Together, these results show how pulsing together with bandpass-like features in a feedback circuit gives rise to surprisingly complex dynamics in the lead-up to sporulation.

According to our model, the emergence of the delayed phase shift depends on the interrelationship between the periodic input to the sporulation circuit and the dynamics of the circuit components. In particular, the phase shift appears when the Spo0A∼P pulse amplitude is high enough to access the repressing part of the transcriptional bandpasses. Thus, the rate of increase of Spo0A∼P determines the number of periods needed for the phase shift to appear. Additionally, in a given period, the magnitude of this rate in comparison to the relative duration of the "ON" phase plays a role in determining the maximal value of Spo0A∼P pulse. If the rate is too slow, then Spo0A∼P pulse is shut off before it reaches a value large enough to generate a phase shift, as seen in the earlier periods. Only if the rate is high enough, does the Spo0A∼P pulse rise to a value large enough to generate a phase shift before it is turned off. These are important considerations as the rate of increase of Spo0A∼P determines the duration of the phase shift, and consequently the timing of the sequence of events leading to the transition to sporulation.

An inherent challenge in the model is to map the relationship between perturbations in the transcriptional bandpasses and the sporulation dynamics. Currently, this is hindered by a limited understanding of how Spo0A∼P interacts with the promoter regions of P_{0A} and P_{0F} to generate the bandpass mode of regulation. An approach that determines how

bandpass regulation is encoded in the promoter architectures will be required to overcome this. This will also be useful in corroborating the parameter estimates reported here or in obtaining more exact ones. In particular, while this study shows that the P_{0A} and P_{0F} transcriptional bandpasses are quantitatively different, further studies may be required to determine the exact ratios of the bandpass thresholds and their slopes. More generally, while the parameters for production-degradation and phosphorylation-dephosphorylation-phosphotransfer used here are reasonable, determining their exact values may require further investigation. Following this, the model can be combined with systematic perturbations to the promoters to develop further insight into the dynamics leading to sporulation initiation.

Studies of terminal differentiation dynamics in individual cells can reveal the fine structure behavior of underlying regulatory circuits. Here, this behavior takes the form of the emergence of a delayed phase shift and the capability, in an alternate state, to suspend the appearance of the phase shift. Fine-structure studies of other circuits regulating terminal differentiation may reveal further instances of temporal order in gene expression. Dynamic single-cell studies of other processes should reveal if constituent genes are sequentially expressed, and if this temporal order is operationally critical or is just a by-product of resource optimization by cells preparing for a terminal state [68].

Chapter 3

Functional Potential of the Core Phosphorelay Architecture

In this chapter, we ask how multiple phosphorelay inputs affect its bandpass characteristics, and, at a more basic level, how phosphotransfer reactions modulate signaling properties inside cells. We address these questions using simple computational models of two-component system architectures. Our results show that the two different types of phosphorelay inputs can be used to independently tune the two bandpass thresholds. Further, we note how the basic phosphotransfer reaction can be used as a building block for linear amplifier-like responses. These results provide broad correlations with design choices in electrical circuits, suggesting that similar considerations have governed the evolution of this architectural diversity.

3.1 Independent Tuning of Bandpass Thresholds

Phosphatases in two-component signaling circuits typically act on the proteins with a receiver domain, and the phosphorelay, with two such proteins, allows the possibility of two phosphatases acting on distinct protein components (Fig. 3.1a). Indeed, the phosphorelay regulating sporulation in *B. subtilis* utilizes this option and has phosphatases that act on Spo0A and Spo0F. Both phosphatases remove phosphates from the relay and are expected to have inhibitory effects on the phosphorelay output Spo0A$\sim$P. In this section, we analyze the effect of their structurally different points of action on the post-translational bandpass. We find that the two phosphatase types shift the bandpass in opposite directions and tune different bandpass thresholds (Fig. 3.1b).

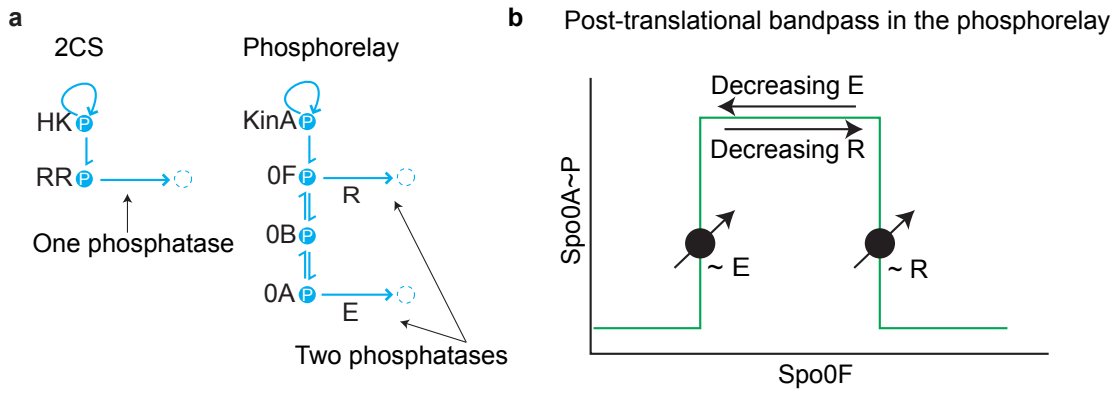

Figure 3.1: Effect of two types of phosphatases on the post-translational bandpass. (a) Canonical two-component system architecture with a histidine kinase (HK) and a response regulator (RR). Phosphorelay architecture with two phosphatases acting on Spo0A and Spo0F, denoted E and R, respectively. (b) Schematic of the effect of modulating phosphatase activities on the post-translational bandpass.

To show this, we used a simple mathematical model, already introduced in Sec. 2.2, to compute the post-translational bandpass response for different activities of the two phosphatases. In the post-translational bandpass response, Spo0A∼P levels are maximal at a unique value of total Spo0F concentration, dependent on the parameters of reaction rates and protein concentrations. For Spo0F levels higher than this value, the effective rate of reverse phosphotransfer away from Spo0A dominates, and diminishes the Spo0A∼P response (Fig. 2.4). The Spo0F phosphatase contributes to this effect by acting as a phosphate drain for the reverse flow of phosphates (Fig. C.1). For simplicity, we assume that the only source of Spo0F dephosphorylation is a phosphatase external to the phosphorelay ($k_h = 0$). This assumption allows a comparison of the two phosphatase activities without the complicating factor of the phosphatase activity of the kinase. Even with this assumption, the post-translational bandpass response is present in this model (Fig. 3.2, green line), and converts to a highpass response in the absence of a Spo0F phosphatase (Fig. 3.2, thick blue line). As expected from this, when the bandpass response is computed for different activities of the Spo0F phosphatase, it shifts towards higher Spo0F values (Fig. 3.2, thin blue lines).

Conversely, for Spo0F levels lower than this value, the effective rate of forward phosphotransfer to Spo0A is limiting, consistent with the notion that Spo0F is essential for phosphates to reach Spo0A. Interestingly, we find that in the absence of the Spo0A phos-

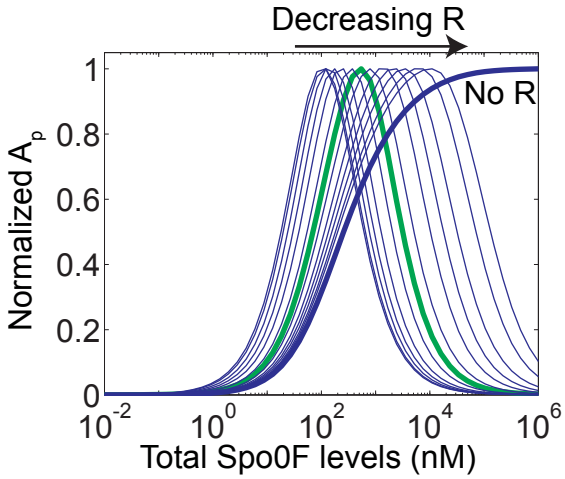

Figure 3.2: Decreasing Spo0F phosphatase activities shift the bandpass response towards higher Spo0F levels. Green line is the post-translational bandpass response curves from the model of the core phosphorelay. Thick blue line is the highpass response in the absence of a Spo0F phosphatase (denoted R, $k_r = 0$). Thin blue lines are bandpass response curves for different values of Spo0F phosphatase activity ($k_r = 10^4/hr$, $k_r = 5 \times 10^3/hr$, $k_r = 2 \times 10^3/hr$, $k_r = 10^3/hr$, $k_r = 5 \times 10^2/hr$, $k_r = 2 \times 10^2/hr$, $k_r = 50/hr$, $k_r = 20/hr$, $k_r = 10/hr$, $k_r = 5/hr$, $k_r = 2/hr$, $k_r = 1/hr$). In each case, the output A_p is normalized by its maximum level.

phatase, low levels (non-zero) of Spo0F do not limit Spo0A∼P levels, and the response is purely lowpass (Fig. 3.3a, thick red line). This behavior can be understood by considering how phosphates are distributed in the Spo0F-Spo0B-Spo0A part of the phosphorelay model, and how phosphate input to the Spo0F-Spo0B-Spo0A part depends on total Spo0F levels.

The distribution of phosphates depends only on the phosphotransfer rates and the Spo0A phosphatase activity, and is given by the following equation,

$$k_t F_p B - k_{-t} F B_p = k_t B_p A - k_{-t} B A_p = k_e A_p.$$

In the absence of the Spo0A phosphatase ($k_e = 0$), this reduces to

$$k_t F_p B - k_{-t} F B_p = k_t B_p A - k_{-t} B A_p = 0. \tag{3.1}$$

This equation can be solved to obtain the dependence of the fraction of phosphorylated

Spo0A on total Spo0F levels.

$$
\begin{aligned}
& k_t B_p A - k_{-t} B A_p = 0, \\
\Longrightarrow \quad & k_t B_p A = k_{-t} B A_p, \\
\Longrightarrow \quad & k_t B_p (A_T - A_p) = k_{-t} B A_p, \\
\Longrightarrow \quad & k_t B_p A_T = (k_t B_p + k_{-t} B) A_p, \\
\Longrightarrow \quad & A_p = A_T \tfrac{k_t B_p}{k_t B_p + k_{-t} B}, \\
\Longrightarrow \quad & \tfrac{A_p}{A_T} = \tfrac{\frac{B_p}{B_T}}{\frac{B_p}{B_T} + \frac{k_{-t}}{k_t}(1 - \frac{B_p}{B_T})}.
\end{aligned} \tag{3.2}
$$

This equation expresses Spo0A∼P in terms of Spo0B∼P. In a similar fashion, Eq. (3.1) can be used to express Spo0B∼P in terms of Spo0F∼P.

$$
\begin{aligned}
& k_t F_p B - k_{-t} F B_p = 0, \\
\Longrightarrow \quad & k_t F_p B = k_{-t} F B_p, \\
\Longrightarrow \quad & k_t F_p (B_T - B_p) = k_{-t} F B_p, \\
\Longrightarrow \quad & k_t F_p B_T = (k_t F_p + k_{-t} F) B_p, \\
\Longrightarrow \quad & B_p = B_T \tfrac{k_t F_p}{k_t F_p + k_{-t} F}, \\
\Longrightarrow \quad & \tfrac{B_p}{B_T} = \tfrac{\frac{F_p}{F_T}}{\frac{F_p}{F_T} + \frac{k_{-t}}{k_t}(1 - \frac{F_p}{F_T})}.
\end{aligned} \tag{3.3}
$$

Together, Eqs. (3.2)–(3.3) can be rearranged to express Spo0A∼P in terms of Spo0F∼P.

$$
\frac{A_p}{A_T} = \frac{\frac{F_p}{F_T}}{\frac{F_p}{F_T} + (\frac{k_{-t}}{k_t})^2 (1 - \frac{F_p}{F_T}).} \tag{3.4}
$$

This expression shows that the fraction of phosphorylated Spo0A is a direct function of the fraction of phosphorylated Spo0F.

The phosphate input to the Spo0F-Spo0B-Spo0A part of the phosphorelay model depends on the balance between the phosphotransfer from KinA to Spo0F and the activity of the Spo0F phosphatase. This balance can be expressed as

$$
k_t K_p F = k_r F_p.
$$

For the given parameters, low Spo0F levels ($F_T << K_T$) mean that this phosphotransfer does not significantly deplete levels of KinA∼P, and is effectively a first-order reaction of Spo0F.

$$\begin{aligned} & K_p \approx K_T, \\ \Longrightarrow \quad & k_t K_T F \approx k_r F_p, \\ \Longrightarrow \quad & k_t K_T (F_T - F_p) \approx k_r F_p, \\ \Longrightarrow \quad & k_t K_T F_T \approx (k_t K_T + k_r) F_p, \\ \Longrightarrow \quad & \frac{F_p}{F_T} \approx \frac{k_t K_T}{k_t K_T + k_r}. \end{aligned} \tag{3.5}$$

Therefore, in this parameter regime, the fraction of phosphorylated Spo0F is independent of the total Spo0F levels. The combined effect of Eqs. (3.4)–(3.5) is that low levels of Spo0F do not affect the levels of Spo0A∼P. As expected from this, when the bandpass response is computed for decreasing Spo0A phosphatase activities, it shifts towards lower Spo0F values (Fig. 3.3a, thin red lines). These results show that the two phosphatases shift the bandpass response in opposite directions (Fig. 3.1b).

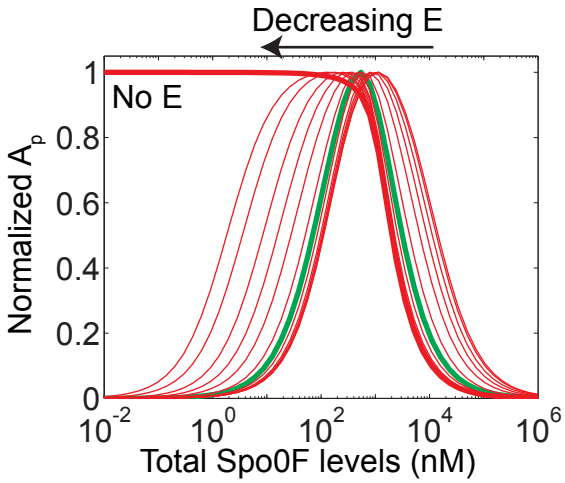

Figure 3.3: Decreasing Spo0A phosphatase activities shift the bandpass response towards lower Spo0F levels. Green line is the post-translational bandpass response curves from the model of the core phosphorelay. Thick red line is the highpass response in the absence of a Spo0A phosphatase (denoted E, $k_e = 0$). Thin red lines are bandpass response curves for different values of Spo0A phosphatase activity ($k_e = 10^4/hr$, $k_e = 5 \times 10^3/hr$, $k_e = 2 \times 10^3/hr$, $k_e = 10^3/hr$, $k_e = 5 \times 10^2/hr$, $k_e = 2 \times 10^2/hr$, $k_e = 50/hr$, $k_e = 20/hr$, $k_e = 10/hr$, $k_e = 5/hr$, $k_e = 2/hr$, $k_e = 1/hr$). In each case, the output A_p is normalized by its maximum level.

There is also a quantitative difference in how these two phosphatases affect the thresholds of the post-translational bandpass response in the above computations. The shift in the higher bandpass threshold as the Spo0F phosphatase activity is varied is an order of magnitude more than the shift in the lower bandpass threshold (Fig. 3.4a). In addition, the shift in the lower bandpass threshold is for bandpasses with low amplitude. Based on these considerations, we conclude that the Spo0F phosphatase exerts a dominant effect on the higher bandpass threshold. Similarly, the shift in the lower bandpass threshold as the Spo0A phosphatase activity is varied is an order of magnitude more than the shift in the higher bandpass threshold (Fig. 3.4b). Further, the shift in the higher bandpass threshold is for bandpasses with low amplitude, suggesting that the Spo0A phosphatase exerts a dominant effect on the lower bandpass threshold. These results show that the two types of phosphatases provide almost independent parameters to tune the two bandpass thresholds (Fig. 3.1b). The presence of these independent tuning knobs is a direct consequence of the phosphorelay architecture.

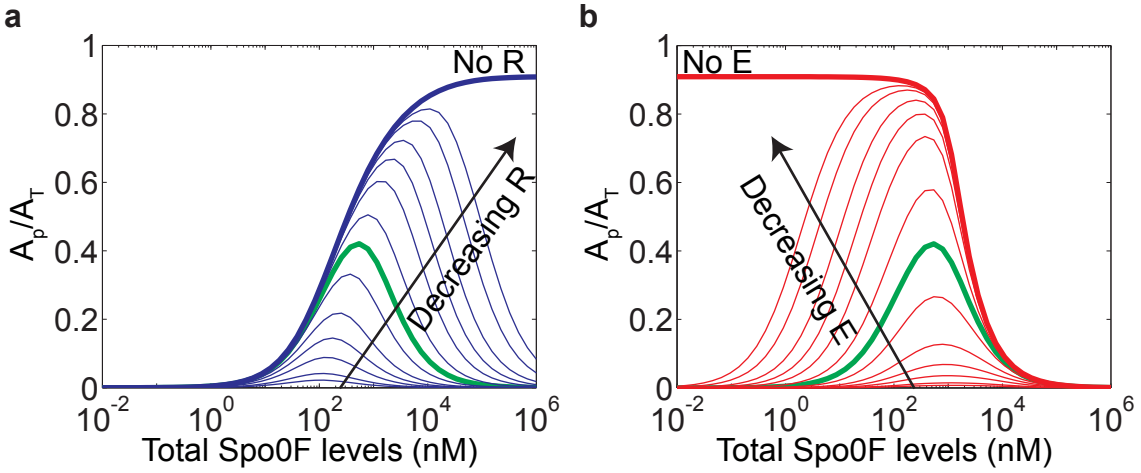

Figure 3.4: Two phosphatases in the phosphorelay independently tune the two thresholds of the post-translational bandpass response. Reproduction of bandpass curves from (a) Fig. 3.2 and (b) Fig. 3.3, with the output A_p normalized by the total protein concentration A_T.

Effect of phosphatase activity of KinA. The above computations assume that Spo0F is dephosphorylated only by an external phosphatase and not by KinA ($k_h = 0$). To understand how the phosphatase activity of KinA affects the dependence of the bandpass response on the phosphorelay phosphatases, we repeated the above computations for two additional cases. First, we examined this dependence when the only source of Spo0F

dephosphorylation is KinA. This allows us to check if the conclusions in the above computations are critically dependent on the assumption $k_h = 0$. Second, we examined whether the phosphatase activity of KinA alters the dependence of the bandpass on the external phosphatases. This allows us to understand the effect of this interaction on the above conclusions.

We find that the bandpass response persists even when the only source of Spo0F dephosphorylation is the phosphatase activity of KinA ($k_r = 0$, Fig. 3.5a, green line), and converts to a highpass response when this is turned off ($k_h = 0$, Fig. 3.5a, thick blue line). As expected from this, when the bandpass response is computed for different phosphatase activities of KinA, it shifts towards higher Spo0F values (Fig. 3.5a, thin blue lines). Further, the shift in the lower bandpass threshold is for bandpasses with low amplitude (Fig. 3.5b). In other words, the phosphatase activity of KinA also exerts a dominant effect on the higher bandpass threshold. These results show that the dependence of the bandpass response on Spo0F phosphatase activity is similar irrespective of whether the source of dephosphorylation is KinA or an external Spo0F phosphatase.

We also checked the dependence of the bandpass response on Spo0A phosphatase activity when Spo0F is dephosphorylated only by KinA. We find that the bandpass response converts to a lowpass response in the absence of the Spo0A phosphatase, and that decreasing Spo0A phosphatase activities shift the bandpass towards lower Spo0F values (Fig. 3.6a). Further, the shift in the higher bandpass threshold is for bandpasses with low amplitude (Fig. 3.6b). In other words, the dominant effect of the Spo0A phosphatase is still on the lower bandpass threshold. As these features are similar to those noted previously (Fig. 3.3), we conclude that the effect of the Spo0A phosphatase activity on the bandpass is also similar irrespective of whether Spo0F is dephosphorylated by KinA or by an external phosphatase.

Next, we considered the modulation of the bandpass by the external phosphatases in the presence of the dephosphorylation of Spo0F by KinA. As both modes of Spo0F dephosphorylation — KinA and external — can regulate the bandpass location and threshold, we expect their relative contribution to determine the extent to which the external phosphatase can modulate these bandpass properties. When the phosphatase activity of KinA is low, the effect of the external Spo0F phosphatase is expected to be similar to the case considered previously, where KinA is not a phosphatase for Spo0F (Fig. 3.2, 3.4a). We find that this is indeed the case (Fig. 3.7a,b). As before, decreasing the activity of the

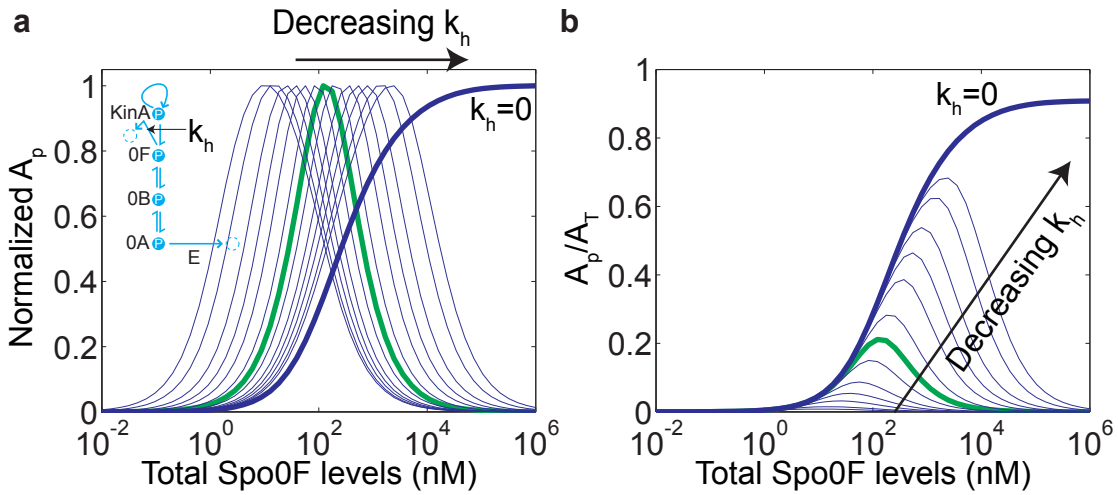

Figure 3.5: Decreasing the phosphatase activity of KinA shifts the bandpass towards higher Spo0F values and exerts a dominant effect on the higher bandpass threshold. (a) Green line is the post-translational bandpass response curves from the model of the core phosphorelay where the only source of Spo0F dephosphorylation is KinA ($k_r = 0$). Legend k_h on the phosphorelay inset denotes this interaction. Thick blue line is the highpass response observed in the absence of this phosphatase activity ($k_h = 0$). Thin blue lines are bandpass response curves for different phosphatase activities of KinA ($k_h = 10^2/(nM \cdot hr)$, $k_h = 50/(nM \cdot hr)$, $k_h = 20/(nM \cdot hr)$, $k_h = 10/(nM \cdot hr)$, $k_h = 5/(nM \cdot hr)$, $k_h = 2/(nM \cdot hr)$, $k_h = 0.5/(nM \cdot hr)$, $k_h = 0.2/(nM \cdot hr)$, $k_h = 0.1/(nM \cdot hr)$, $k_h = 0.05/(nM \cdot hr)$, $k_h = 0.02/(nM \cdot hr)$, $k_h = 0.01/(nM \cdot hr)$). In each case, the output A_p is normalized by its maximum level. (b) Bandpass response curves from (a) are replotted with the output A_p normalized by the total protein concentration A_T.

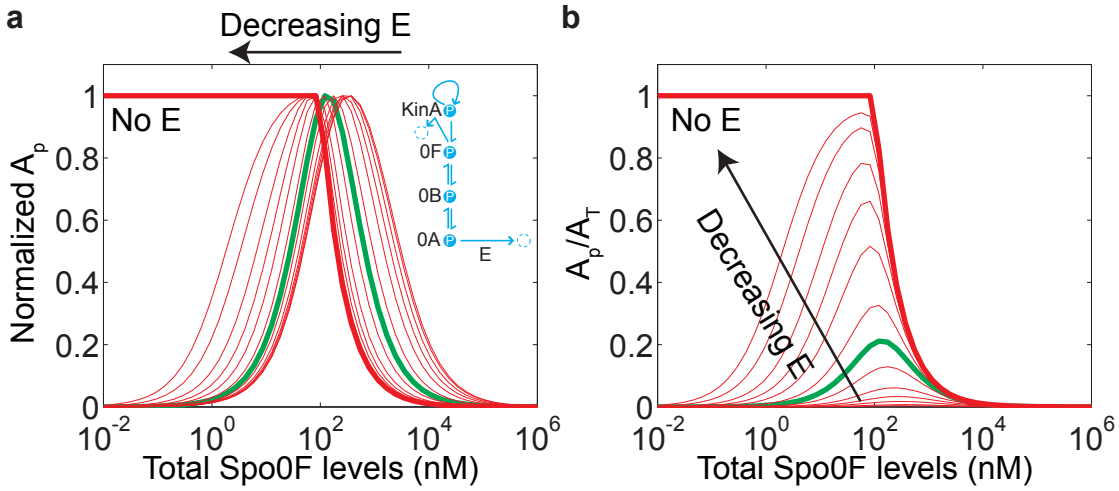

Figure 3.6: Decreasing Spo0A phosphatase activities shift the bandpass response towards lower Spo0F levels and exert a dominant effect on the lower bandpass threshold even when Spo0F is dephosphorylated by KinA. (a) Green line is the post-translational bandpass response curves from the model of the core phosphorelay where the only source of Spo0F dephosphorylation is KinA ($k_r = 0$). Thick red line is the highpass response in the absence of a Spo0A phosphatase (denoted E, $k_e = 0$). Thin red lines are bandpass response curves for different values of Spo0A phosphatase activity ($k_e = 10^4/hr$, $k_e = 5 \times 10^3/hr$, $k_e = 2 \times 10^3/hr$, $k_e = 10^3/hr$, $k_e = 5 \times 10^2/hr$, $k_e = 2 \times 10^2/hr$, $k_e = 50/hr$, $k_e = 20/hr$, $k_e = 10/hr$, $k_e = 5/hr$, $k_e = 2/hr$, $k_e = 1/hr$). In each case, the output A_p is normalized by its maximum level. (b) Bandpass response curves from (a) are replotted with the output A_p normalized by the total protein concentration A_T.

external Spo0F phosphatase shifts the bandpass towards higher Spo0F values (Fig. 3.7a). Further, the external Spo0F phosphatase continues to exert a dominant effect on the higher bandpass threshold (Fig. 3.7b). A minor difference, however, is that bandpass does not convert into a highpass response when the external Spo0F phosphatase activity is turned off (Fig. 3.7a, thick blue line). This is along expected lines as a bandpass will exist as long as there is dephosphorylation of Spo0F, which in this case is through KinA. In contrast, when the phosphatase activity of KinA is high, we find that the external Spo0F phosphatase has little effect on the bandpass location or threshold (Fig. 3.7c,d). This is because the principal contribution to the net Spo0F phosphatase activity, which modulates these bandpasss properties, is through KinA and not the external phosphatase. Therefore, the modulation of the bandpass location and threshold by an external Spo0F phosphatase is effective when the phosphatase activity of KinA is low.

Finally, we note that the effect of the Spo0A phosphatase on the bandpass doesn't depend significantly on the strength of the KinA phosphatase (Fig. 3.8), and is similar to the cases considered previously (Figs. 3.3, 3.4b and 3.6).

3.2 Linear Amplifier-like Responses

In this section, we investigate the role of the phosphotransfer reaction in modulating the input-output response. We characterize its effect on the sensitivity (s) of response, estimated by the relative change of output (y) with respect to the input (x). The sensitivity can be obtained by computing the logarithmic derivative of the input-output response,

$$s = \frac{\partial \log y}{\partial \log x}.$$

This measure highlights the difference between a switch-like response and an amplifier-like response (Fig. 3.9). For a switch-like response, the sensitivity is extremely high near the switching threshold and very small away from this threshold. In contrast, the sensitivity for an amplifier-like response is constant throughout the range of input/output. We find that the phosphotransfer reaction can increase the range of sensitivity of the response, allowing two-component systems to operate as signaling amplifiers.

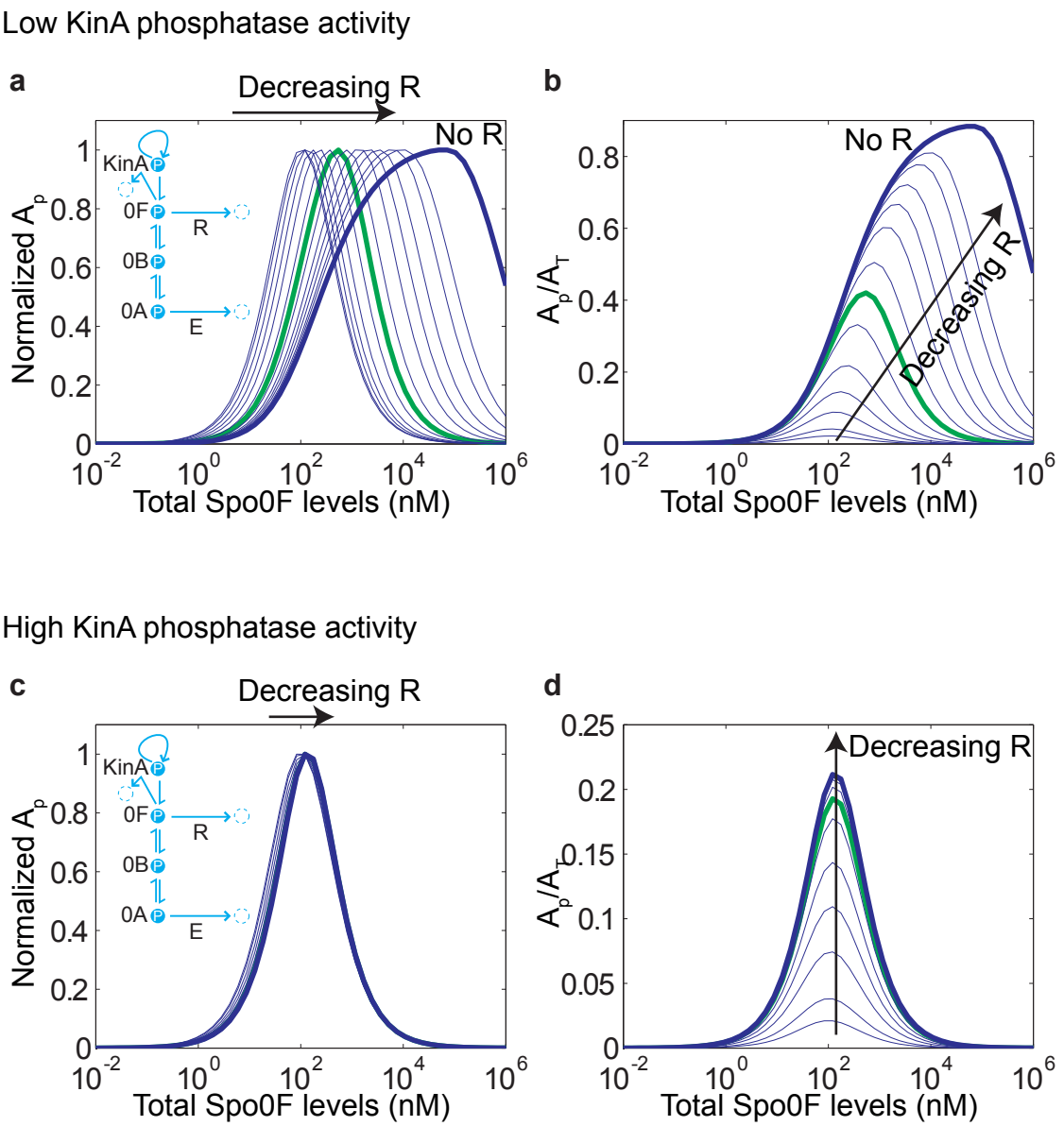

Figure 3.7: Bandpass regulation by external Spo0F phosphatase activity depends on the phosphatase activity of KinA. (a) Green line is the bandpass response from the model of the core phosphorelay with a low phosphatase activity of KinA ($k_h = 1 \times 10^{-4}/(nM \cdot hr)$). Thick blue line is the bandpass response in the absence of an external Spo0F phosphatase (denoted R, $k_r = 0$). Thin blue lines are bandpass response curves for different values of the external Spo0F phosphatase activity ($k_r = 10^4/hr$, $k_r = 5 \times 10^3/hr$, $k_r = 2 \times 10^3/hr$, $k_r = 10^3/hr$, $k_r = 5 \times 10^2/hr$, $k_r = 2 \times 10^2/hr$, $k_r = 50/hr$, $k_r = 20/hr$, $k_r = 10/hr$, $k_r = 5/hr$, $k_r = 2/hr$, $k_r = 1/hr$). In each case, the output A_p is normalized by its maximum level. (b) Bandpass response curves from (a) are replotted with the output A_p normalized by the total protein concentration A_T. (c) Bandpass response curves from (a) are replotted for a high phosphatase activity of KinA ($k_h = 1/(nM \cdot hr)$). (d) Bandpass response curves from (c) are replotted with the output A_p normalized by the total protein concentration A_T.

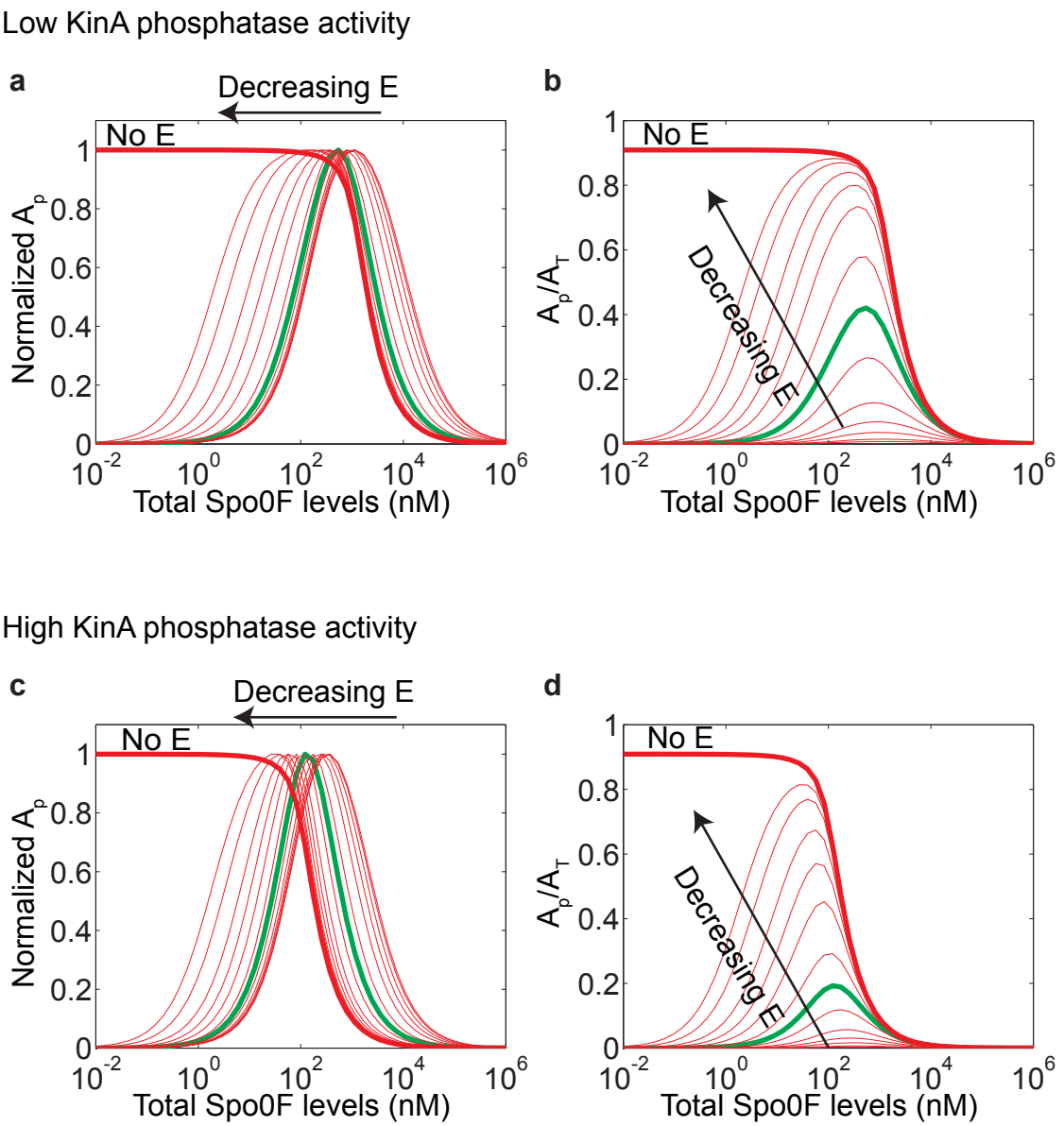

Figure 3.8: Bandpass regulation by Spo0A phosphatase activity does not significantly depend on the phosphatase activity of KinA. (a) Green line is the bandpass response from the model of the core phosphorelay with a low phosphatase activity of KinA ($k_h = 1 \times 10^{-4}/(nM \cdot hr)$). Thick red line is the highpass response in the absence of a Spo0A phosphatase (denoted E, $k_e = 0$). Thin red lines are bandpass response curves for different values of Spo0A phosphatase activity ($k_e = 10^4/hr$, $k_e = 5 \times 10^3/hr$, $k_e = 2 \times 10^3/hr$, $k_e = 10^3/hr$, $k_e = 5 \times 10^2/hr$, $k_e = 2 \times 10^2/hr$, $k_e = 50/hr$, $k_e = 20/hr$, $k_e = 10/hr$, $k_e = 5/hr$, $k_e = 2/hr$, $k_e = 1/hr$). In each case, the output A_p is normalized by its maximum level. (b) Bandpass response curves from (a) are replotted with the output A_p normalized by the total protein concentration A_T. (c) Bandpass response curves from (a) are replotted for a high phosphatase activity of KinA ($k_h = 1/(nM \cdot hr)$). (d) Bandpass response curves from (c) are replotted with the output A_p normalized by the total protein concentration A_T.

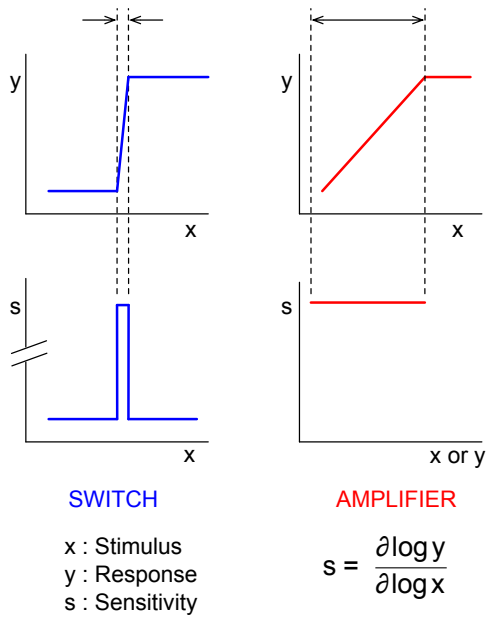

Figure 3.9: Idealized stimulus-response curves and sensitivity profiles of a switch (blue) and an amplifier (red).

3.2.1 Two-Component System

Before investigating the dependence of the two-component system sensitivity profiles on the phosphotransfer reaction, we introduce, for comparison purposes, a hypothetical one-component system model. The one-component system consists of a protein, whose phosphorylated form (denoted R_p) functions as the output response and the unphosphorylated form (R) is the input sensor. We model the response of a 1CS using the simple mass action kinetics,

$$\frac{dR_p}{dt} = k_s(R_T - R_p) - k_h R_p.$$

Here, $R_T = R + R_p$ is the total concentration, k_s is the rate of phosphorylation that acts as the input stimulus, and k_h is the rate of dephosphorylation. At steady state,

$$\frac{dR_p}{dt} = 0 \implies R_p = R_T \frac{k_s}{k_s + k_h}.$$

For this input-output response, the sensitivity can be expressed analytically as

$$s = \frac{\partial \log R_p}{\partial \log k_s} = \frac{k_h}{k_s + k_h} = 1 - \frac{R_p}{R_T}.$$

These expressions show that the sensitivity (s) decreases as the input (k_s) is increased, or, equivalently, as the output levels (R_p) increase (Fig. 3.10, black). Because the sensing and response functions are encoded on the same molecule, an increase in the output (R_p) automatically reduces the sensor levels (R). This consideration limits the range of linear sensitivity ($s \approx 1$) in a 1CS.

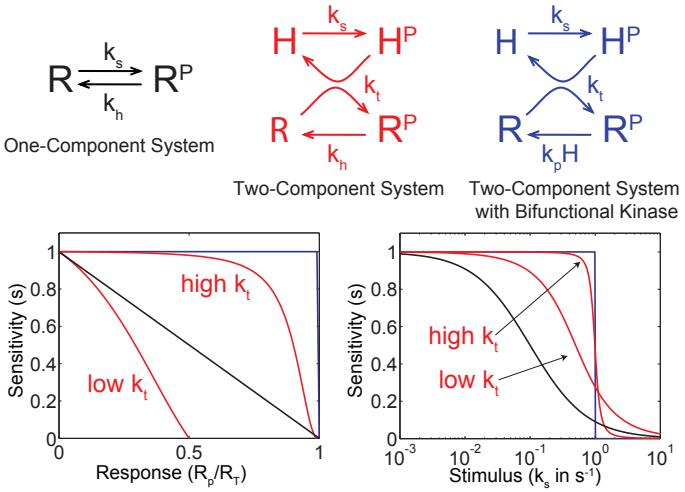

Figure 3.10: Phosphotransfer can enhance range of linear sensitivity. Black, red, and blue lines indicate the sensitivity profiles from models of the one-component system, the two-component system, and the two-component system with a bifunctional kinase, respectively. Parameters: H_T=10nM, R_T=$10^2 nM$, k_h=$10^{-1}s^{-1}$, k_p=k_h/H_T, low k_t=$10^{-2}/(nM \cdot s)$, high k_t=$10^0/(nM \cdot s)$.

Now, we compute the sensitivity in a two-component system model, in which the sensing and response functions necessarily reside on two separate protein components. The two-component system model has three reactions: autophosphorylation of the sensor kinase (H), phosphotransfer from the phosphorylated sensor kinase (H_p) to the response regulator (R), and dephosphorylation of the phosphorylated regulator (R_p),

$$\begin{aligned} \frac{dH_p}{dt} &= k_s(H_T - H_p) - k_t H_p(R_T - R_p), \\ \frac{dR_p}{dt} &= k_t H_p(R_T - R_p) - k_h R_p. \end{aligned}$$

Here, H_T and R_T are total concentrations, k_s is the rate of autophosphorylation (and the input stimulus), k_t is the rate of phosphotransfer, and k_h is the rate of dephosphorylation. For this model, the steady state condition results in a quadratic equation in R_p that can be numerically solved to compute the input-output response (R_p vs k_s) and the corresponding

sensitivity profile. We find that, in the limit of fast phosphotransfer ($k_t H_T > k_h$), the range of linear sensitivity in the input stimulus and in the output range is enhanced from that possible in a 1CS (Fig. 3.10, red). This is because rapid phosphotransfer shuttles phosphates away from the sensor (H_p) to the response regulator (R), thereby freeing up sensor (H) to detect further changes in input.

Next, we investigated the role of a bifunctional kinase on the response sensitivity. For this we augmented the two-component system model so that the dephosphorylation of the response regulator is mediated by the unphosphorylated sensor kinase (H),

$$\begin{aligned} \frac{dH_p}{dt} &= k_s(H_T - H_p) - k_t H_p(R_T - R_p), \\ \frac{dR_p}{dt} &= k_t H_p(R_T - R_p) - k_p(H_T - H_p)R_p. \end{aligned}$$

Here, k_h is the rate of kinase-dependent dephosphorylation of the response regulator. The steady state input-output response for this model is

$$R_p = \begin{cases} \frac{k_s}{k_p} & \text{if } k_s < k_p R_T, \\ R_T & \text{if } k_s > k_p R_T. \end{cases}$$

The sensitivity of this response is

$$s = \begin{cases} 1 & \text{if } k_s < k_p R_T, \\ 0 & \text{if } k_s > k_p R_T. \end{cases}$$

Therefore, the response in this model is perfectly linear as long as it is unsaturated (Fig. 3.10, blue). The linear response in the model of a two-component system with a bifunctional kinase is consistent with the trend of linear sensitivity discussed for the two-component system model.

3.2.2 Phosphorelay

Based on the increased range of linear sensitivity with the addition of a single rapid phosphotransfer step, it is reasonable to expect a further enhancement with a cascade of similarly rapid phosphotransfer steps. To test this, we augmented the two-component system model

with the addition of two more protein components to make a four-component system model. In the four-component system model, phosphate is transferred sequentially from the sensor kinase (H) to the response regulator (R) via intermediatory proteins T and D,

$$\begin{aligned}
\frac{dH_p}{dt} &= k_s(H_T - H_p) - k_t H_p(D_T - D_p), \\
\frac{dD_p}{dt} &= k_t H_p(D_T - D_p) - k_t D_p(T_T - T_p), \\
\frac{dT_p}{dt} &= k_t D_p(T_T - T_p) - k_t T_p(R_T - R_p), \\
\frac{dR_p}{dt} &= k_t T_p(R_T - R_p) - k_h R_p.
\end{aligned}$$

Here, the steady state condition results in a quartic equation that can be numerically solved to obtain the input-output response and the corresponding sensitivity profile. For the same parameters as the two-component system model, we find that the sensitivity profile for this input-output response is linear for a larger range (Fig. 3.11). The enhanced linearity is because each stage in the cascade shuttles phosphate to the next stage, thereby staying free (unphosphorylated) to detect further changes in the effective stage input. Therefore, we find that one consequence of phosphotransfer reactions is that they can enhance the range of linear sensitivity.

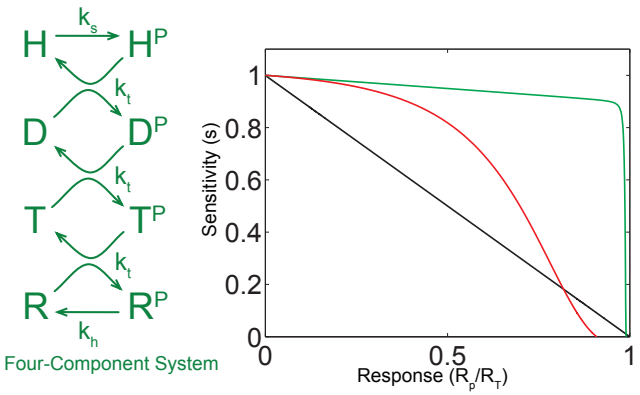

Figure 3.11: Phosphorelay can further increase the range of linear sensitivity. Sensitivity profiles of a one-component system (red), a two-component system (black), and a four-component system (green). Four-component system parameters: H_T=10nM, R_T=$10^2 nM$, k_h=$10^{-1}s^{-1}$, k_t=$10^{-1}/(nM \cdot s)$, D_T=T_T=R_T.

Linear input-output response in a similar phosphorelay model has been recently reported [15]. The approach used is complementary to the one presented here, and focuses

on comparison of the signaling response across different stages of the phosphorelay.

Robustness of the output to protein concentrations. These results present an investigation of the input-output sensitivity of some two-component signaling architectures. Another signaling property that has the potential to be functionally useful is the robustness of the output to changes in concentrations of the protein components. In fact, previous investigations of this in the context of the two-component system with a bifunctional kinase have noted that the output can be robust to the concentrations of the response regulator and of the kinase [7, 51, 54]. Here, we examine the presence of this robustness property in the models discussed above. We note that this robustness property is also present in the model of the two-component system with a bifunctional kinase described here. In particular, there are two regimes in this model (Fig. 3.12a): one, at low R_T levels, where the output is saturated and so depends on R_T, and two, at high R_T levels, where the output is independent of R_T. The steady state output values in this figure are computed by numerically integrating the model equations for increasing levels of R_T. Robustness to a parameter requires integral feedback attenuating the effect of that parameter, and the phosphatase activity of the kinase has been identified as a key element of the feedback mechanism providing robustness to changes in protein concentrations [54]. It is illustrative to compare this behavior with that of the one-component system model. In this case, the output is not robust to R_T (Fig. 3.12b, generated by numerical integration). Therefore, there is no feedback in this model that makes the output robust to changes in the concentration of the response regulator.

Motivated by the existence of this robustness property in the two-component model with a bifunctional kinase, we examined its existence in the model of the simple two-component system architecture, where the kinase does not possess the phosphatase activity. To investigate this, we computed the steady state output values by numerically integrating the equations for increasing levels of R_T. We find a robustness property that is similar to the one in the model with a bifunctional kinase (Fig. 3.12c): at low R_T levels, the output is dependent on R_T, and at high R_T levels, the output is largely independent of R_T. While the transition between these two regimes is not as sharp as the one in the model with a bifunctional kinase, there is a regime where the output is almost robust to the concentration of the response regulator. The only difference between this model and the one-component system model, which doesn't have this robustness property, is the phosphotransfer reaction. This suggests that phosphotransfer is a key element of the feedback mechanism providing

robustness to R_T. We find that the four-component system model, which has a cascade of phosphotransfers, also has this robustness property (Fig. 3.12d, generated by numerical integration). Similar output robustness properties also exist with respect to the concentration of the histidine kinase in the models of two-component system with the bifunctional kinase (see also [7, 51, 54]), the simple two-component system, and the four-component system (Fig. 3.13), as well as with respect to the other phosphotransfer proteins in the four-component system model (Fig. 3.14). Therefore, these models of two-component system architectures have regimes where the output is robust to the protein concentrations.

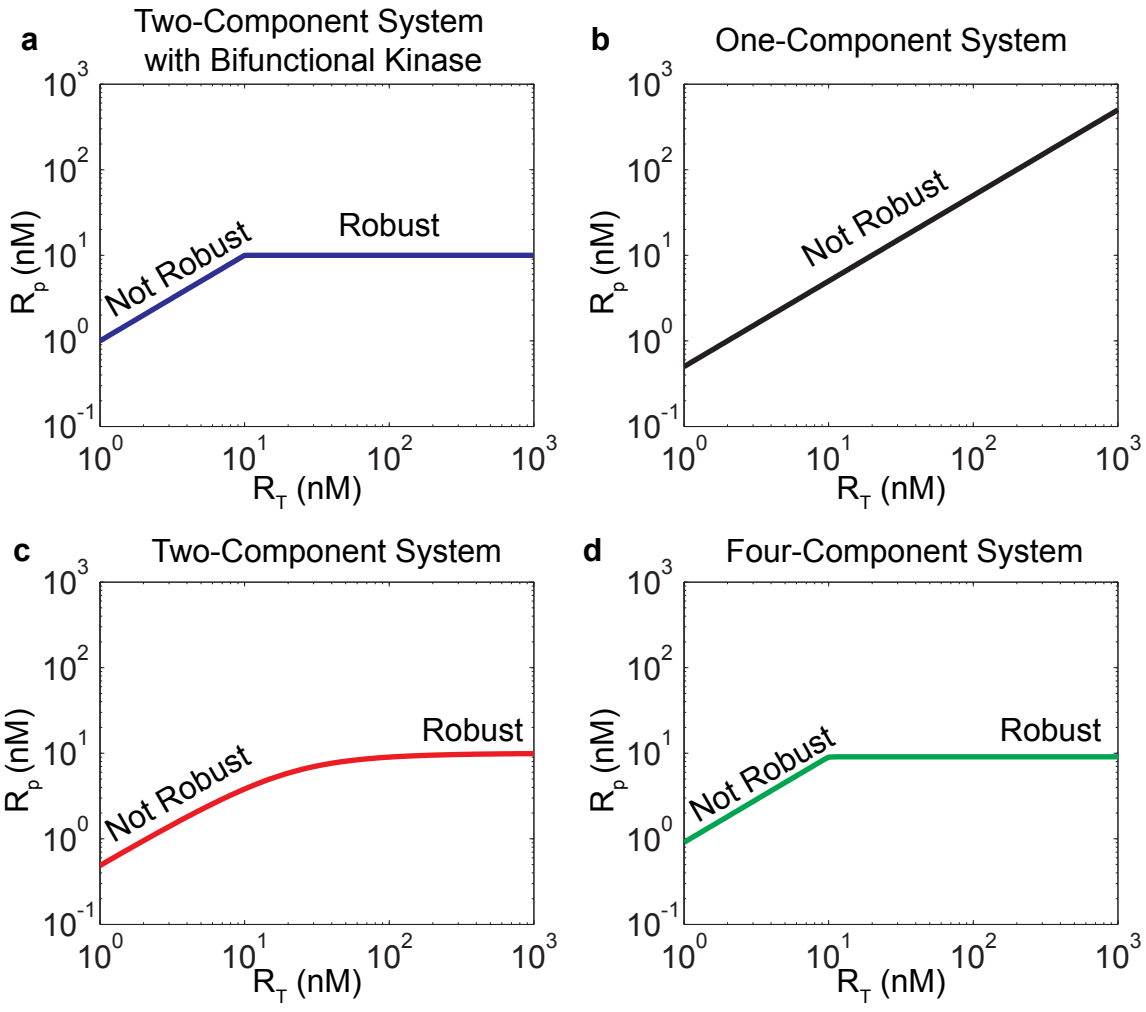

Figure 3.12: Output can be robust to R_T in two-component system architectures. Dependence on the output (R_p) on the concentration of the response regulator (R_T) for models of (a) two-component system with a bifunctional kinase, (b) one-component system, (c) two-component system, and (d) four-component system. Parameters: H_T=10nM, D_T=T_T=$10^2 nM$, k_h=$10^{-1} s^{-1}$, k_p=k_h/H_T, k_t=$10^{-2}/(nM \cdot s)$.

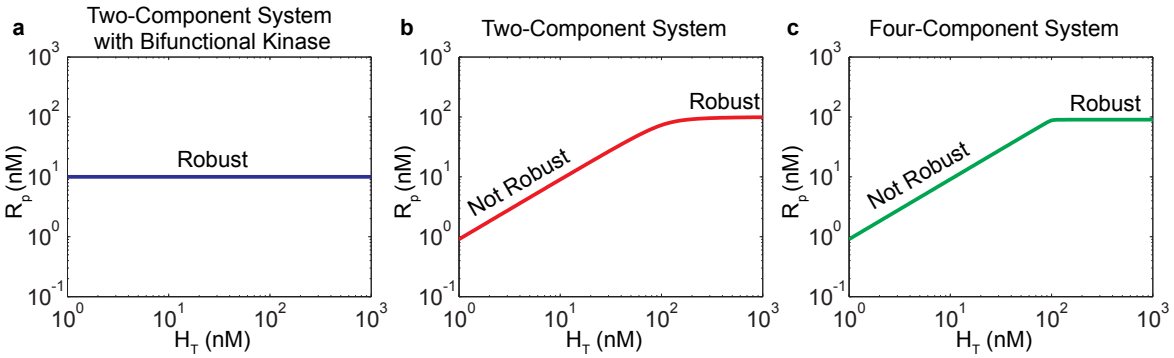

Figure 3.13: Output can be robust to H_T in two-component system architectures. Dependence on the output (R_p) on the concentration of the histidine kinase (H_T) for models of (a) two-component system with a bifunctional kinase, (b) two-component system, and (c) four-component system. Parameters: H_T=$10nM$, R_T=D_T=T_T=10^2nM, k_h=$10^{-1}s^{-1}$, k_p=$10^{-2}/(nM\cdot s)$, k_t=$10^{-2}/(nM\cdot s)$.

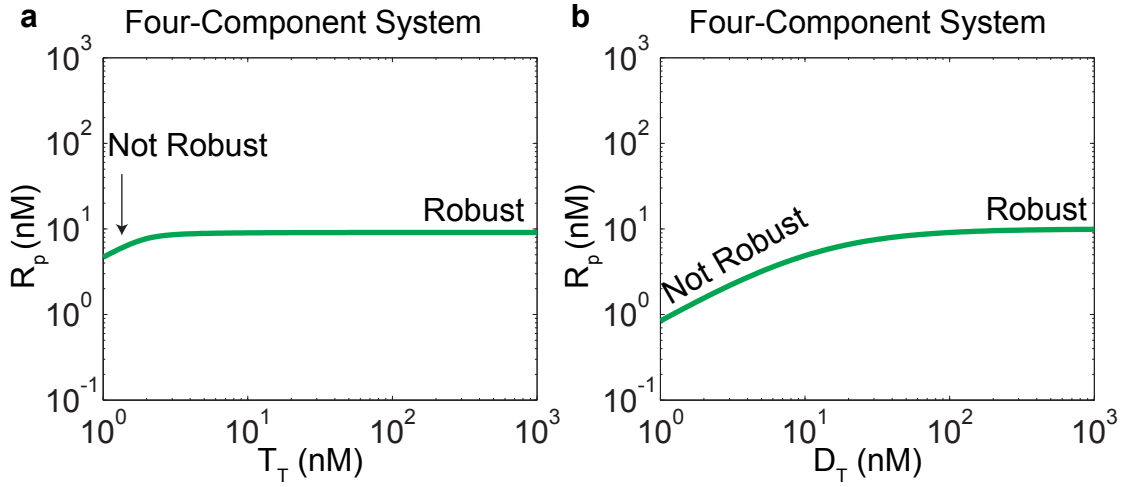

Figure 3.14: Output can be robust to intermediatory phosphotransfer proteins in the four-component system architecture. Dependence on the output (R_p) in the four-component system model on (a) the concentration of T_T for D_T=10^2nM and (b) the concentration of D_T for T_T=10^2nM. Other parameters: H_T=$10nM$, R_T=10^2nM, k_h=$10^{-1}s^{-1}$, k_t=$10^{-2}/(nM\cdot s)$.

Phosphotransfer reactions in hybrid architectures can enhance the range of ultrasensitivity. Phosphotransfer reactions analyzed so far have been intermolecular, from one protein to another. Additionally, phosphotransfer can also occur intramolecularly, between two domains of the same protein. Signaling architectures with such hybrid proteins are called hybrid architectures. To understand how phosphotransfer reactions affect signaling properties of hybrid phosphorelays, we computed their input-output responses. Some aspects of the reaction mechanisms in the hybrid proteins are not clearly known. For example, consider a hypothetical two-component system architecture consisting of a hybrid kinase AB, and a response regulator C. It is not clear if all possible phosphoforms — AB, A_pB, AB_p, A_pB_p — exist. Assuming they do, it is not clear whether the phosphoforms (AB_p, A_pB_p) are equally capable of phosphotransfer to C. Consequently, certain additional assumptions are required before computing the input-output response.

To analyze the response sensitivity here, we first assumed that the phosphoform A_pB_p exists and is the only state that transfers phosphates to C (Fig. 3.15). This reaction scheme has three types of reactions: autophosphorylation of AB and AB_p, phosphotransfer from A_pB to AB_p and from A_pB_p to C, and dephosphorylation of AB_p and C_p,

$$\begin{aligned}
\frac{d[A_pB]}{dt} &= k_s(AB_T - [A_pB] - [AB_p] - [A_pB_p]) - k_t[A_pB] + k_1C[A_pB_p], \\
\frac{d[AB_p]}{dt} &= -k_2[AB_p] + k_t[A_pB] - k_s[AB_p], \\
\frac{d[A_pB_p]}{dt} &= -k_2[AB_p] + k_t[A_pB] - k_s[AB_p], \\
\frac{dC_p}{dt} &= k_1C[A_pB_p] - k_hC_p.
\end{aligned}$$

Here, AB_T and C_T are total concentrations, k_s is the rate of autophosphorylation (and the input stimulus), k_t is the rate of phosphotransfer from A_pB to AB_p, k_1 is the rate of phosphotransfer from A_pB_p to C, k_2 is the rate of dephosphorylation of AB_p, and k_h is the rate of dephosphorylation of C_p. For this model, we use numerical integration to investigate the steady state input-output responses (C_p vs k_s). We find that it is possible to generate an enhanced range of quadratic sensitivity (s≈2, Fig. 3.15), through a mechanism similar to the linear responses discussed above. This can be explained as follows: As the phosphoform A_pB_p has two phosphates, it requires two cycles of input to reach it. This increases the maximum absolute sensitivity from 1, as in previous models, to 2. Next, a

rapid phosphotransfer rate can increase the range of this ultrasensitivity ($s > 1$) via the same phosphate-shuttling mechanism as in the models above. So, the quadratic sensitivity arises due to the multiple phosphorylation assumption and the extended range of quadratic sensitivity is due to rapid phosphotransfer. Therefore, this response is conceptually similar to the amplifier-like responses in models of 2CS architectures.

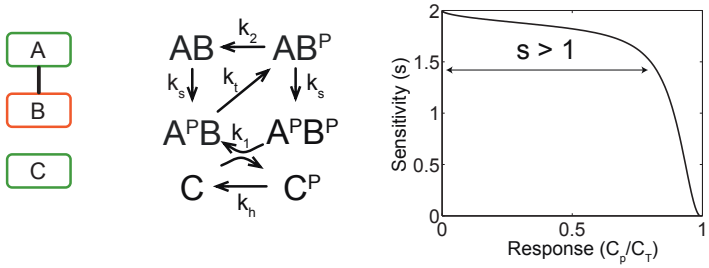

Figure 3.15: Enhanced range of quadratic sensitivity in a hybrid phosphorelay reaction scheme. Parameters for the response curve: $AB_T = 10nM$, $C_T = 100nM$, $k_t = 10s^{-1}$, $k_1 = 10^{-1}/(nM \cdot s)$, $k_2 = 10s^{-1}$, $k_h = 10^{-2}s^{-1}$, k_s is varied in the range $10^{-3}s^{-1}$–$10^{1}s^{-1}$.

Next, we considered the case where the roles of the phosphoforms AB_p and A_pB_p are switched, so that AB_p transfers phosphates to C (Fig. 3.16). This reaction scheme has the same reactions as above, except for the phosphotransfer from AB_p to C and the dephosphorylation of A_pB_p,

$$\begin{aligned}
\frac{d[A_pB]}{dt} &= k_s(AB_T - [A_pB] - [AB_p] - [A_pB_p]) - k_t[A_pB] + k_1[A_pB_p], \\
\frac{d[AB_p]}{dt} &= -k_2C[AB_p] + k_t[A_pB] - k_s[AB_p], \\
\frac{d[A_pB_p]}{dt} &= -k_2C[AB_p] + k_t[A_pB] - k_s[AB_p], \\
\frac{dC_p}{dt} &= k_2C[A_pB_p] - k_hC_p.
\end{aligned}$$

Here, k_2 is the rate of phosphotransfer from AB_p to C, and k_1 is the rate of dephosphorylation of A_pB_p. For this model, we use numerical integration to investigate the steady state input-output responses (C_p vs k_s). We find that it is possible to generate a non-monotonic response (Fig. 3.16). This can be explained as follows: As stimulus levels increase, the phosphoform AB_p is populated earlier than the phosphoform A_pB_p. For further increase in stimulus levels, all of the sensor kinase is in the A_pB_p phosphoform and the population of AB_p decreases. Therefore, the phosphoform AB_p has a non-monotonic response to the

stimulus levels. As phosphotransfer is from AB_p to C, this non-monotonic profile is reflected in the response regulator output. Therefore, a non-monotonic response is also possible in this hybrid kinase architecture.

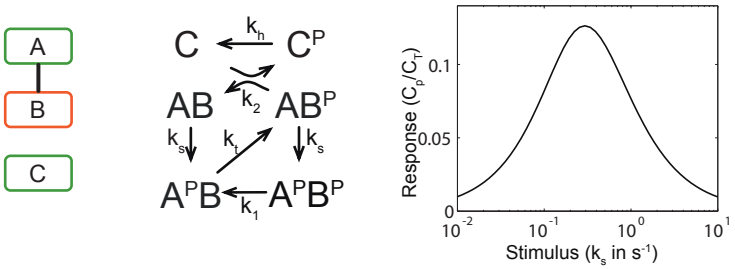

Figure 3.16: Non-monotonic response in a hybrid phosphorelay reaction scheme. Parameters for the reaction scheme: $AB_T = 10nM$, $C_T = 100nM$, $k_t = 10^0 s^{-1}$, $k_1 = 10^{-2} s^{-1}$, $k_2 = 10/(nM \cdot s)$, $k_h = 10^{-1} s^{-1}$.

3.3 Analogies to Electrical Circuits

Here, we have explored the functional potential of the phosphorelay, an architectural variant of the family of two-component system circuits. Using simple computational models, we find that: One, the two types of phosphatases in the phosphorelay can be used by the cell to shift the post-translational bandpass in different directions, and to independently tune its two thresholds in a quantitative fashion. Two, the phosphotransfer reaction, a basic building block of two-component system architectures, can be used to design linear signaling amplifiers. These results suggest ways in which cells can harness the functional potential of different two-component system architectures.

Tuning parameters are an important aspect of electrical circuits, typically used to optimize the design for different operating conditions. These can be used in static scenarios, such as in tuning bandpass thresholds to detect a band of voltage levels, or in dynamic scenarios, such as in tuning gains of adaptive controllers. In fact, response curves in electrical circuits used to detect voltage bands are analogous to the post-translational bandpass discussed above. Similarly, linearity in amplifier response can also be an important consideration in electrical circuits, as in sound systems, where deviations from linearity introduce distortion in the output. The requirement for linearity is especially important in cases where the input signal has a large dynamic range. In particular, simple linear amplifiers constructed

using electronic op-amps are analogous to two-component systems with linear amplifiers in their use of feedback. Negative feedback is used to generate linear input-output profiles in an electronic op-amp. In an analogous fashion, negative feedback, encoded via the phosphotransfer reaction, can enhance the range of linear sensitivity in simple two-component systems.

The consumption of power is a significant constraint in the design of electrical circuits. Given their broad analogies with electrical circuits, power consumption may also be a challenge in the evolution of two-component signaling circuits. It will be interesting to characterize the rates of power consumption across different two-component system architectures. This may highlight design tradeoffs in signaling circuits, and provide insights into the architectural diversity of two-component signaling systems.

Computational studies of signaling circuits can reveal properties that have the potential to be functionally used by the cell. Here, these properties include independent tuning parameters for different aspects of the response, as well as ways to generate linear amplifier-like responses. Juxtaposing these circuits against their distribution in various cellular contexts will be instructive in understanding if and how these properties are used. The growing number of two-component signaling circuits in bacteria being identified by recent genome sequencing and annotation efforts offers a useful starting point for this [65]. These data have already highlighted a correlation between the number of such signaling circuits and genome size [2], suggesting that these circuits are needed to encode complex signal processing tasks. This is also supported by the broad correlation that exists between the complexity of a phosphotransfer configuration and the enormity of the cellular function that it encodes [5]. Further investigations of how these circuits operate in their natural contexts may reveal other instances of potentially useful properties, and will be required to determine if such properties are essential or merely by-products of molecular interactions used to implement cellular signaling.

Chapter 4

Conclusion

4.1 Summary of Contributions

Biological processes, spanning scales from individual proteins to entire ecosystems, exhibit significant temporal organization. Widely occurring examples at the scale of individual cells include self-repeating cycles of circadian rhythms, and transitions from one state to another observed during differentiation. Explaining how these cellular behaviors are implemented through dynamic interactions between genes and proteins is a fundamental biological question. Analogous to their roles in the analysis and design of temporal patterns throughout engineering and science, methods of dynamics and control have provided significant insight into this problem. However, two recent developments — large-scale characterization of molecular components, and new methods to visualize these interactions over time — present an opportunity to revisit this fundamental problem and offer more complete solutions. Recent examples of this include a study of transient differentiation, where excitable dynamics in the underlying circuit naturally explain the observed pulse-like phenomena [58], and chemotaxis, where the identification of integral feedback control in the molecular circuit is a key design principle in understanding how robust performance arises from inherently noisy components [67].

In this thesis, we study whether and how temporal ordering of events is implemented in terminal differentiation, using the canonical example of sporulation in *B. subtilis*. Progression to sporulation can occur over multiple cell generations, after which an ordered sequence of events remodels the cell into a dormant spore. The underlying molecular circuit, consisting of a phosphorelay embedded in transcriptional feedback loops, has been extensively characterized, and exhibits several features that are striking from a dynamical systems point

of view, including bandpass interactions coupled together in feedback loops, and modulated periodically in a cell-cycle-dependent fashion. However, how these nonlinear time-varying features combine to generate patterns of gene expression during the sporulation progression is unclear.

Here, we have addressed this issue by combining dynamical models with single-cell time-lapse fluorescent microscopy techniques. We have characterized the bandpass interactions between circuit components. Based on these measurements, we have constructed a simple mathematical model and analyzed it under conditions of periodic input, which mimic cell-cycle modulation effects in real cells. The model predicts the emergence of a delayed phase shift between circuit components, whose existence we verify experimentally. The model also predicts an alternate cellular state that can be accessed using a genetic perturbation, and we have shown that similar behavior can be observed experimentally. Lastly, we have used computational models to explore the significance of the phosphorelay architecture in the context of simpler options available in the superfamily of two-component signaling systems. We have shown how the phosphorelay architecture enables two types of inputs that can independently regulate different aspects of its response, as well as how phosphotransfer building blocks can be used to construct signaling amplifiers.

4.2 Future Work

4.2.1 Systematic perturbation of bandpass responses in sporulation progression

Given that coupled bandpass feedback loops can generate dynamic patterns during sporulation progression, a natural question to ask is how sporulation progression depends on the underlying dynamical patterns and bandpass characteristics. This is important in further understanding how initiation of sporulation depends on the dynamic interactions in the phosphorelay circuit. Addressing this question will require a combined experimental-modeling approach. On the experimental side, a prerequisite is to determine the mechanism of the transcriptional bandpasses. How gene regulation functions are encoded in the DNA sequence of the promoter has been previously investigated in prokaryotic contexts (lac, lambda), and may serve as a useful template for this. Following this, native promoters in the sporulation circuit need to be replaced by promoters with altered bandpass characteris-

tics. The current mathematical model, or more complete versions of it, can serve as a tool to identify which of the bandpass characteristics are most likely to change circuit dynamics and have a significant impact on sporulation progression. A more complete understanding of how sporulation progression depends on the phosphorelay circuit, likely to arise from such an investigation, will be an important step towards understanding similar processes in other bacterial species.

4.2.2 Role of temporally ordered gene expression in formation of the asymmetric septum

In many types of cells, the decision to initiate differentiation is followed by mechanical rearrangements of cellular structures. While dynamic single-cell studies have characterized gene expression during decision-making as well as during mechanical rearrangements, the coordination between these processes is unclear. For example, the first major morphological development after the initiation of sporulation in *B. subtilis* is a switch from medial cell division to the formation of an asymmetric septation. Not only is this switch regulated by the phosphorelay circuit, but it also occurs immediately after initiation. While it has been shown that the phosphorelay circuit can generate temporal order in the activation of target genes, it is not clear if such temporal order is relevant for the formation of the asymmetric septum. Medial cell division involves the formation of a FtsZ ring at the mid-point of the cell. While the transition from medial cell division to asymmetric septation is not completely known, there are several striking features associated with this: One, the medial FtsZ ring translocates to the asymmetric septation at sporulation initiation. Two, this transition can be triggered even in vegetatively growing cells harboring an extra copy of the FtsZ gene by the induction of a FtsZ-associated protein SpoIIE. Three, during sporulation initiation, FtsZ and SpoIIE are upregulated by low and high levels of Spo0A$\sim$P, respectively. We propose to investigate if the phosphorelay circuit encodes the following sequential order of events: First, a translocation of the FtsZ ring away from the medial position. Second, stabilization of the FtsZ ring by SpoIIE at a distal position. To check if this is the case, we will develop a mathematical model of the FtsZ-SpoIIE dynamics and test it with different times of activation of FtsZ relative to SpoIIE. We expect a specific FtsZ-SpoIIE time-lag to be an optimum choice for asymmetric septation, with deviations from this generating altered locations or spurious septation. Furthermore, examination of the underlying mechanisms

may reveal sources of robustness in this process. An alternative possibility is that there is temporal order in this process, but that it is an instance of resource optimization rather than of an operational requirement. Such a study is relevant to other processes where mechanical rearrangements follow initiation, for example in the germinal vesicle breakdown in oocyte maturation [66], or in the formation of whorls during flowering [34]. This study should also shed light on fundamental physical processes of symmetry-breaking, as in which of the two polar positions of the FtsZ ring is eventually chosen, and scaling, as in the positional invariance of the asymmetric septum for different cell sizes that can arise in different environments or in other related species.

4.2.3 Power consumption in two-component signaling architectures

Power consumption is an important constraint in the design of electrical circuits. Typically, performance capabilities of a circuit are limited both by the energy required and the heat generated during operation. Based on operational similarities between 2CS and electrical circuits, power consumption may also be a constraint in the evolution of signaling circuits in cell biology. Phosphorylation-based signaling circuits are ideal for studying this phenomenon, as the identity of the energy source (ATP) is known. Further, the family of two-component signaling circuits presents a diversity of architecture and possibly function that can be used to get a broader perspective on the problem. Therefore, an investigation of how power is consumed across different two-component architectures is likely to yield significant insights into cellular signaling. We propose to approach this problem computationally, using simple models of two-component system architectures to calculate power consumption. Motivated by engineering considerations, we expect power consumption to be directly related to the information transferred, or the bandwidth, of the signaling response. Results from this study are likely to highlight tradeoffs between power consumption and signaling efficacy in cells. Complementarily, how cellular signaling circuits operate under these power constraints may serve as a guiding principle in proposing energy-efficient architectures for use in engineering contexts.

Appendix A

Materials and Methods

All strains were constructed using standard *B. subtilis* protocols and molecular biology methods (Table A.1). The background of all strains used was *B. subtilis* PY79. For image segmentation, a constitutive promoter expressing fluorescent protein reporter RFP was chromosomally integrated into PY79 (LS1). Promoter fusions to fluorescent proteins were chromosomally integrated using *Bacillus* integration vectors pDL30, ECE174 (both from lab stocks), and pER82 (kindly provided by Jonathan Dworkin). We also used the antibiotic-switching plasmid ECE73 (*cmR*→*neoR*). The integration vector 174hs (from lab stock) containing the IPTG-inducible LacI system added to the ECE174 backbone was used to induce Spo0F to different levels. For copy number perturbation, the plasmid pHP13 (from lab stock) was used. Based on these, other plasmids for promoter fusions and for circuit perturbations were constructed with *Escherichia coli* DH5α or DH5αZ1 by using standard methods of PCR, restriction enzyme digests, and ligations (Table A.2, A.3),

i. The plasmid pSS938 was constructed by ligating the EcoRI-BamHI fusion PCR fragment P_{0A}-YFP and pDL30 cut with EcoRI-BamHI. The fusion PCR fragment P_{0A}-YFP was made by fusing P_{0A} (primers oss80967, oss80949 and template PY79) and YFP (primers oss80944, oss80147 from a template plasmid containing YFP from lab stock) using primers oss80967, oss80147.

ii. The plasmid pSS925 was constructed by ligating the BamHI-EcoRI fusion PCR fragment P_{0F}-CFP and ECE174 cut with EcoRI-BamHI. The fusion PCR fragment P_{0F}-CFP was made by fusing P_{0F} (primers oss80973, oss80972 and template PY79) and CFP (primers oss80975, oss80146 from a template plasmid containing CFP from lab stock) using primers oss100436, oss80146.

iii. The plasmid pSS711 was constructed by ligating the EcoRI-BamHI PCR fragment *spo0F* (primers oss80907, oss80181 and template PY79) and pHP13 cut with EcoRI-BamHI.

iv. The plasmid pSS1027 was constructed by ligating the EcoRI-BamHI fusion PCR fragment P_{hyp}-CFP and ECE174 cut with EcoRI-BamHI. The fusion PCR fragment P_{hyp}-CFP was made by fusing P_{hyp} (primers oss100801, oss100805 and template MF2158) and CFP (primers oss100804, oss100802 from a template plasmid containing CFP from lab stock) using primers oss100801, oss100802.

v. The plasmid pSS916 was constructed by ligating the EcoRI-BamHI fusion PCR fragment P_{0F}-YFP and pDL30 cut with EcoRI-BamHI. The fusion PCR fragment P_{0F}-YFP was made by fusing P_{0F} (primers oss80973, oss100437 and template PY79) and YFP (primers oss100438, oss80147 from a template plasmid containing YFP from lab stock) using primers oss100436, oss80147.

vi. The plasmid pSS1025 was constructed by ligating the EcoRI-BamHI fusion PCR fragment P_{0F}-YFP and pER82 cut with EcoRI-BamHI. The fusion PCR fragment P_{0F}-YFP was made as above.

vii. The plasmid pSS1031 was constructed by ligating the HindIII-NheI fusion PCR fragment Spo0F-CFP and 174hs cut with HindIII-NheI. The fusion PCR fragment Spo0F-CFP was amplified (primers oss100908, oss100905) from a vector already containing a Spo0F-CFP fragment, which was made by fusing the Spo0F gene (primers oss80900, oss80913 and template PY79) and CFP (primers oss80912, oss100802 from a template plasmid containing CFP from lab stock) using primers oss80900, oss100802.

viii. The *spo0F* deletion PCR was made by fusing the gene conferring *specR* with flanking regions bearing homology upstream and downstream of the Spo0F coding region. The primer pairs (oss80928, oss80924), (oss80922,oss80923) and (oss80925,oss80927) were used to PCR *specR* (pDL30 template), upstream homology region (PY79 template) and downstream homology region (PY79 template), respectively. These pieces were then fused using primers oss80922 and oss80927.

Number	Strain	Reference/Source/Construction
MF2158	PY79 *spo0A*::*specR*::*cmR* P_{lacI}-LacI P_{hyp}-$0A^{sad67}$	Lab stock
LS1	PY79 *ppsB*::*ermR* P_{trpE}-RFP	Lab stock
LS4	PY79	Lab stock
SS813	PY79 *ppsB*::*ermR* P_{trpE}-RFP *spo0A*::*specR*::*cmR* P_{lacI}-LacI P_{hyp}-$0A^{sad67}$	MF2158 → LS1
SS1039	PY79 *sacA*::*cmR* P_{hyp}-CFP	pSS1027 → LS4
SS1060	PY79 *sacA*::*cmR*::*neoR* P_{hyp}-CFP	ECE73 → SS1039
SS1075	PY79 *ppsB*::*ermR* P_{trpE}-RFP *spo0A*::*specR*::*cmR* P_{lacI}-LacI P_{hyp}-$0A^{sad67}$ *sacA*::*cmR*::*neoR* P_{hyp}-CFP	SS1060 → SS813
SS1125	PY79 *ppsB*::*ermR* P_{trpE}-RFP *spo0A*::*specR*::*cmR* P_{lacI}-LacI P_{hyp}-$0A^{sad67}$ *sacA*::*cmR*::*neoR* P_{hyp}-CFP *amyE*::*specR* P_{0A}-YFP	pSS916 → SS1075
SS1017	PY79 *ppsB*::*ermR* P_{trpE}-RFP *amyE*::*specR* P_{0F}-YFP	pSS938 → LS1
SS1019	PY79 *ppsB*::*ermR* P_{trpE}-RFP *amyE*::*specR* P_{0F}-YFP *spo0A*::*specR*::*cmR* P_{lacI}-LacI P_{hyp}-$0A^{sad67}$	MF2158 → SS1017
SS1106	PY79 *ppsB*::*ermR* P_{trpE}-RFP *amyE*::*specR* P_{0F}-YFP *spo0A*::*specR*::*cmR* P_{lacI}-LacI P_{hyp}-$0A^{sad67}$ *sacA*::*cmR*::*neoR* P_{hyp}-CFP	SS1060 → SS1019
SS946	PY79 *ppsB*::*ermR* P_{trpE}-RFP *sacA*::*cmR* P_{0F}-CFP	pSS925 → LS1
SS1007	PY79 *ppsB*::*ermR* P_{trpE}-RFP *sacA*::*cmR* P_{0F}-CFP *amyE*::*specR* P_{0A}-YFP	pSS916 → SS946
SS1021	PY79 *ppsB*::*ermR* P_{trpE}-RFP *sacA*::*cmR*::*neoR* P_{0F}-CFP *amyE*::*specR* P_{0A}-YFP	ECE73 → SS1007
SS1023	PY79 *ppsB*::*ermR* P_{trpE}-RFP *sacA*::*cmR*::*neoR* P_{0F}-CFP *amyE*::*specR* P_{0A}-YFP pHP13-*spo0F*	pSS711 → SS1021
SS745	PY79 *spo0F*::*specR*	*spo0F* deletion PCR → LS4
SS843	PY79 *ppsB*::*ermR* P_{trpE}-RFP *spo0F*::*specR*	SS745 → LS1
SS1037	PY79 *ppsB*::*ermR* P_{trpE}-RFP *spo0F*::*specR* *amyE*::*neoR* P_{0F}-YFP	pSS1025 → SS843
SS1064	PY79 *ppsB*::*ermR* P_{trpE}-RFP *spo0F*::*specR* *amyE*::*neoR* P_{0F}-YFP *sacA*::*cmR* P_{lacI}-LacI P_{hyp}-Spo0F-CFP	pSS1031 → SS1037

Table A.1: List of strains.

Number	Plasmid
pSS916	pDL30 P_{0A}-YFP
pSS925	ECE174 P_{0F}-CFP
pSS711	pHP13-*spo0F*
pSS1027	ECE174 P_{hyp}-CFP
pSS938	pDL30 P_{0F}-YFP
pSS1031	174hs Spo0F-CFP
pSS1025	pER82 P_{0F}-YFP

Table A.2: List of plasmids.

Number	Primer Sequence (5'-3')
oss80146	ATA GAATTC AAAAGGCTGAACCCTAAGGT
oss80147	GAT GGATCC GCAATGATGAACCAGTAAGAGTAGC
oss80967	ACT GAATTC CAGAAGCAGGAATCGATATTTATGG
oss80949	CAACGCCGGTGAACAGTTCTTCACCTTTGCTCAT GTTTCTTCCTCCCCAAATGTAGTTAA
oss80944	GTGAATCCTGTTAACTACATTTGGGGAGGAAGAAAC ATGAGCAAAGGTGAAGAACTGTTC
oss80973	GGCCTGCTGGTAATCGCAGGCCTTTTTTATT AATCCTCCTTTATAACGTACAATATCAGTA
oss100436	CAC GGATCC GGCCTGCTGGTAATCGCAGGCCTTTTTTATTAATCCTCCTTTATAACGTACA
oss80972	AACTCCAGTGAAAAGTTCTTCTCCTTTACGCAT ATTCATCATTTTACACCCCAATATTAT
oss80975	CGAAAATCATAATATTGGGGTGTAAAATGATGAAT ATGCGTAAAGGAGAAGAACTTTTCA
oss80907	AGC GGATCC AAGTGAATCCTCCTTTATAACGTACAATA
oss80181	ATA GAATTC GTCAGTTAGACTTCAGGGGCAGAT
oss100801	TAT GAATTC GACTCTCTAGCTTGAGGCATCAAATAA
oss100805	AACTCCAGTGAAAAGTTCTTCTCCTTTACGCAT AGTAGTTCCTCCTTATGTGTCGACTAA
oss100804	AATTAAGCTTAGTCGACACATAAGGAGGAACTACT ATGCGTAAAGGAGAAGAACTTTTCA
oss100802	ATA GGATCC AAAAGGCTGAACCCTAAGGT
oss100436	CAC GAATTC GGCCTGCTGGTAATCGCAGGCCTTTTTTATT AATCCTCCTTTATAACGTACA
oss100437	AACGCCGGTGAACAGTTCTTCACCTTTGCTCAT ATTCATCATTTTACACCCCAATATTAT
oss100438	ACGAAAATCATAATATTGGGGTGTAAAATGATGAAT ATGAGCAAAGGTGAAGAACTGTTC
oss100908	ATA AAGCTT ACATAAGGAGGAACTACT ATGATGAATGAAAAAATTTTAATCGTTG
oss100905	ATA GCTAGC AAAAGGCTGAACCCTAAGGT
oss80900	ATA GAATTC AGTGAATCCTCCTTTATAACGTACAATAT
oss80913	TGAAAAGTTCTTCTCCTTTACGCATGTTAGACTTCAGGGGCAGATATTTT
oss80912	AAAATATCTGCCCCTGAAGTCTAAC ATGCGTAAAGGAGAAGAACTTTTCA
oss80922	TATCAGGATGAAGTGGTGTACGAGC
oss80927	TAACTGTTTCTTTGATCGCTTCACG
oss80924	CGAAAATCATAATATTGGGGTGTAAACATATGCAAGGGTTTATTGTTTTCTAA
oss80923	TTAGAAAACAATAAACCCTTGCATATGTTTACACCCCAATATTATGATTTTCG
oss80925	ATGTATTCACGAACGAAAATCGATCAAAAAGAAGAAACAAATGAATCATG
oss80928	CATGATTCATTTGTTTCTTCTTTTTGATCGATTTTCGTTCGTGAATACAT

Table A.3: List of primers.

Appendix B

Movie Protocols

Time-lapse microcopy. Cells to be imaged were inoculated in CH media and grown overnight in a 30°C shaking water incubator. They were then diluted 1:40 into fresh CH media and grown for 2–3 hours so that the OD600 was in the range 0.5–0.7. Following this, they were resuspended 1:1 in Sterlini-Mandelstam (SM) media after two washes in SM. 0.5ul of this was spotted on an appropriate pad (0.5mm x 0.5mm), allowed to dry, and flipped onto a glass-bottom dish (Wilco). The dish was sealed with parafilm to reduce pad evaporation during imaging. The pads were made from SM media mixed with 1.5% Low Melting Point Agarose (Omni). Required amount of inducer IPTG was added to the pads.

Progression to sporulation was imaged at 37°C using a microscope automated for time-lapse fluorescence data acquisition. Images were acquired every 10 minutes on a Nikon Eclipse-Ti inverted microscope fitted with a perfect focus system, ASI motorized stage, Photometrix Coolsnap HQ2 camera, Sutter Lambda LS Xenon Arc lamp, and controlled from a computer using MetaMorph.

Data analysis. The fluorescence values and lengths in single cells were extracted with customized segmentation and tracking algorithms coded in MATLAB and C. Promoter activity per unit length (P) was calculated from the measured mean fluorescence value (M) and cell lengths (L) using the formula

$$P(t) = \frac{dM}{dt} + \frac{1}{L}\frac{dL}{dt}M(t).$$

The derivative was computed from a smoothened version of the mean fluorescence and cell length. For this, mean fluorescence was smoothened with a moving average filter and length

was fitted to a second-order polynomial. To plot the transcriptional bandpass characteristics, time traces up to the initiation of sporulation, as seen from the appearance of a fluorescent dark spot at the tip of the cell, were used. For the post-translational bandpass, the peak P_{0F} pulse amplitude was measured from $T = 0$ minutes to $T = 600$ minutes, and the steady state Spo0F-CFP level was measured at $T = 500$ minutes. For measurements of phase shift between P_{0A} and P_{0F}, promoter activity pulses with peak amplitude greater than a threshold ($0.1 a.u.$) were used.

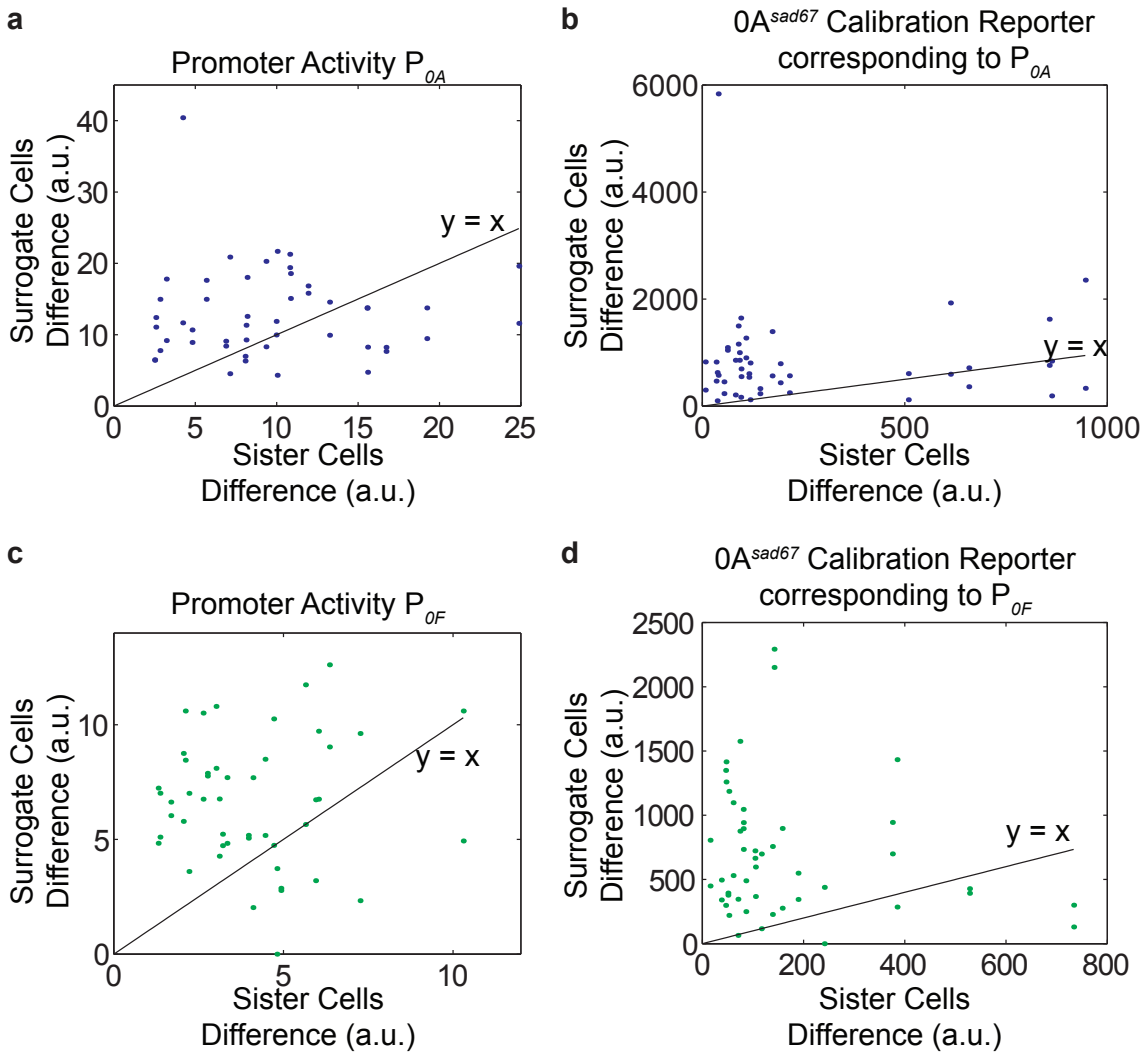

Figure B.1: Variability between sister cells is typically smaller than between randomly chosen sister cell pairs. Difference between a cell and its sister and between the same cell and a randomly chosen surrogate sister cell is calculated for traces of (a) P_{0A}, (b) Spo0A^{sad67} calibration reporter corresponding to the P_{0A} bandpass measurement, (c) P_{0F}, and (d) Spo0A^{sad67} calibration reporter corresponding to the P_{0F} bandpass measurement. Each dot represents one cell, and has co-ordinates (x, y), where x is the difference between sister cells and y is the difference between surrogate cells. Difference metric for two given traces $u(t)$ and $v(t)$ is, $d(u, v) = \sum_{t=0}^{T} |u(t) - v(t)|$, where T is the minimum of the durations of the two traces. In each case, most points lie above the straight line $y = x$, indicating that the difference between sister cells is smaller than between surrogate sister cells.

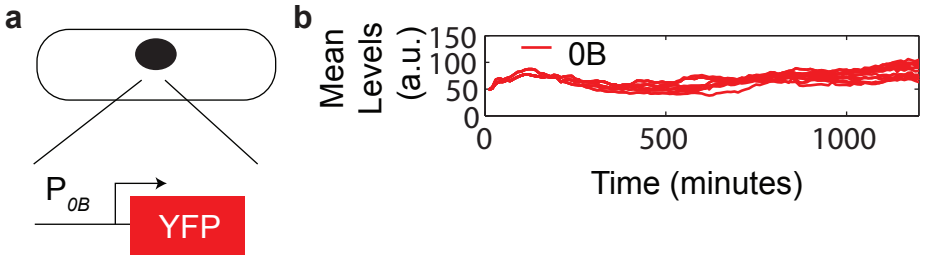

Figure B.2: Mean fluorescence of a P_{0B} reporter changes less than twofold during sporulation initiation. (a) Schematic of the strain with a YFP fluorescent reporter fused to P_{0B}. The strain uses the plasmid ECE174 P_{0B}-YFP (from lab stocks) integrated into an LS1 background. Imaging was done as described in the methods section, but on an Olympus IX-81 inverted microscope fitted with an ASI motorized stage, Hamamatsu Orca-ER camera, Sutter Lambda LS Xenon Arc lamp, and controlled using a combined Visual Basic - ImagePro software. (b) Mean fluorescence levels are non-zero at the start and change less than twofold during sporulation initiation.

Appendix C

Analysis of Models

Mathematical modeling was done in MATLAB. Nullclines in the two-dimensional model were computed from the zero contour of the surface functions $P_{0A}(A_T, F_T) - \gamma A_T$ and $P_{0F}(A_T, F_T) - \gamma F_T$. Ordinary differential equations were solved in MATLAB using integrator ode23s. The dependence of Spo0A∼P on Spo0F levels in the model without feedback and pulsing was computed by simulating the equations for a time longer than the timescale of the system. In the simulation of the two-dimensional model, A_p was computed at each timestep by simulating the equation of the phosphorylated proteins using the current values of A_T, B_T, F_T, K_T, and $k_s(ON/OFF)$.

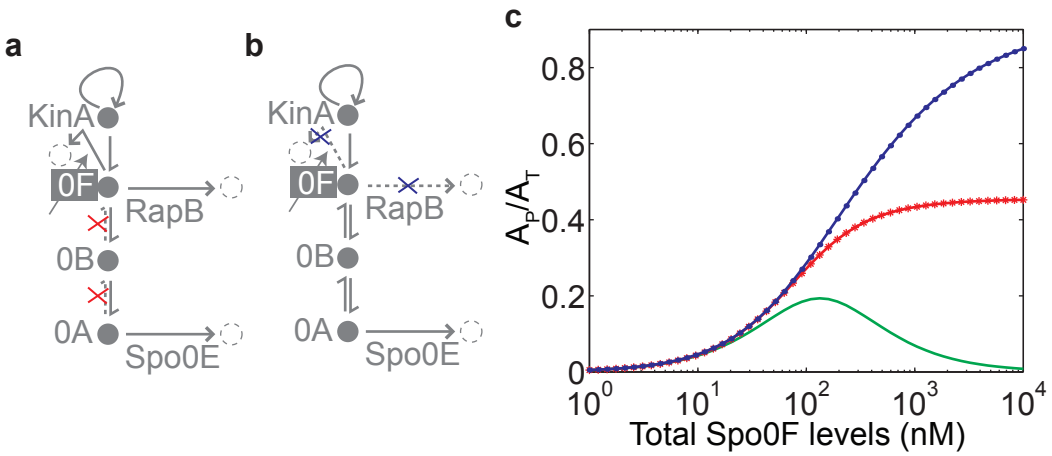

Figure C.1: Post-translational bandpass in the model is due to drain of Spo0A phosphates via reverse phosphotransfer and Spo0F phosphatases. Diagrams of the core phosphorelay with no reverse phosphotransfer (a, red) and no Spo0F phosphatase (b, blue), for which the post-translational Spo0F bandpass computation is performed from the simple phosphorelay model (no pulsing or transcriptional feedbacks). Both curves are plotted in (c), along with the curve from Fig. 2.4 (green).

Post-translational Spo0F bandpass in a more complex model of the core phosphorelay. This supplementary information describes a model of core phosphorelay with a more complicated reaction scheme that that described in the main text. The post-translational Spo0F bandpass discussed in the main text is based on a simple model of the core phosphorelay. In principle, a more complicated reaction scheme involving reaction intermediates is also possible. Here, we verify the post-translational Spo0F bandpass results in a model of the core phosphorelay that contains these reaction intermediates. Such reaction schemes have been previously used for phosphorelay-like signaling systems [54]. This model consists of 17 variables, of which eight correspond to the phosphoforms of the four phosphorelay proteins — K, K_p, F, F_p, B, B_p, A, A_p. In addition there are two additional variables corresponding to the free levels of the phosphatases of Spo0A and Spo0F, denoted E and R, respectively. Finally, there are seven additional variables corresponding to the reaction intermediates involved in the phosphorylation, phosphotransfer, and dephosphorylation reactions — $[K_pF]$, $[F_pB]$, $[B_pA]$, $[KT]$, $[KTF_p]$, $[F_pR]$, $[A_pE]$. Here, the variable T denotes ATP, which is assumed to be maintained at a constant value by the cell. Consequently, $[KT]$ is the KinA-ATP intermediate that mediates autophosphorylation and $[KTF_p]$ is the $[KT]$-Spo0F intermediate that mediates the dephosphorylation of Spo0F. These variables are not independent as they are constrained by the total concentrations of these proteins. There are six such constraints,

$$\begin{aligned}
A_T &= A + A_p + [B_pA] + [A_pE], \\
B_T &= B + B_p + [B_pA] + [F_pB], \\
F_T &= F + F_p + [F_pB] + [K_pF] + [KTF_p] + [F_pR], \\
K_T &= K + K_p + [KTF_p] + [K_pF] + [KT], \\
R_T &= [F_pR] + R, \\
E_T &= [A_pE] + E.
\end{aligned}$$

Here, A_T, B_T, F_T, K_T, R_T, and E_T denote the total concentrations of Spo0A, Spo0B, Spo0F, KinA, RapB, and Spo0E, respectively. Because of these six constraints, there are 11 free variables that described the system, and are chosen to be K, K_p, F, F_p, B, B_p, A, A_p, $[K_pF]$, $[F_pR]$, $[A_pE]$. The remaining variables can be expressed as a combination of

these variables and the total concentrations,

$$\begin{aligned}
[B_pA] &= A_T - A - A_p - [A_pE], \\
[F_pB] &= B_T - B - B_p - [B_pA], \\
[KTF_p] &= F_T - F - F_p - [F_pB] - [K_pF] - [F_pR], \\
[KT] &= K_T - K - K_p - [KTF_p] - [K_pF], \\
R &= R_T - [F_pR], \\
E &= E_T - [A_pE].
\end{aligned}$$

The equations corresponding to these reactions are

$$\begin{aligned}
\frac{dK}{dt} &= -Tk_1K + k_{1p}[KT] + \nu_K[K_pF], \\
\frac{dK_p}{dt} &= k_s[KT] - k_2K_pF + k_{2p}[K_pF], \\
\frac{dF}{dt} &= -k_2K_pF + k_{2p}[K_pF] + \nu_P[KTF_p] + k_5p[F_pB] - k_5FB_p + \nu_R[F_pR], \\
\frac{dF_p}{dt} &= \nu_K[K_pF] - k_3[KT]F_p + k_{3p}[KTF_p] - k_4F_pB + k_{4p}[F_pB] - k_8F_pR + k_8p[F_pR], \\
\frac{dB}{dt} &= -k_4F_pB + k_{4p}[F_pB] + k_{7p}[B_pA] - k_7BA_p, \\
\frac{dB_p}{dt} &= k_{5p}[F_pB] - k_5FB_p - k_6B_pA + k_{6p}[B_pA], \\
\frac{dA}{dt} &= -k_6B_pA + k_{6p}[B_pA] + \nu_E[A_pE], \\
\frac{dA_p}{dt} &= k_{7p}[B_pA] - k_7BA_p - k_9A_pE + k_{9p}[A_pE], \\
\frac{d[K_pF]}{dt} &= k_2K_pF - (k_{2p} + \nu_K)[K_pF], \\
\frac{d[F_pR]}{dt} &= k_8F_pR - (k_{8p} + \nu_R)[F_pR], \\
\frac{d[A_pE]}{dt} &= k_9A_pE - (k_{9p} + \nu_E)[A_pE].
\end{aligned}$$

Here, the rate constants assigned to the different reactions are as follows,

i. Autophosphorylation of K: k_1,k_{1p} are the association-dissociation rates for the reaction intermediate $[KT]$, and k_s is the rate of formation of K_p from this reaction intermediate.

ii. Phosphotransfer from K_p to F: k_2,k_{2p} are the association-dissociation rates for the reaction intermediate $[K_pF]$, and ν_K is the rate of formation of F_p from this reaction

intermediate.

iii. Dephosphorylation of F_p by $[KT]$: k_3,k_{3p} are the association-dissociation rates for the reaction intermediate $[KTF_p]$, and ν_P is the rate of formation of F from this reaction intermediate.

iv. Phosphotransfer from F_p to B: k_4,k_{4p} are the association-dissociation rates for the reaction intermediate $[F_pB]$ from the reactants F_p and B.

v. Reverse phosphotransfer from B_p to F: k_5,k_{5p} are the association-dissociation rates for the reaction intermediate $[F_pB]$ from the reactants B_p and F.

vi. Phosphotransfer from B_p to A: k_6,k_{6p} are the association-dissociation rates for the reaction intermediate $[B_pA]$ from the reactants B_p and A.

vii. Reverse phosphotransfer from A_p to B : k_7,k_{7p} are the association-dissociation rates for the reaction intermediate $[B_pA]$ from the reactants A_p and B.

viii. Dephosphorylation of F_p by R: k_8,k_{8p} are the association-dissociation rates for the reaction intermediate $[F_pR]$, and ν_R is the rate of formation of F from this reaction intermediate.

ix. Dephosphorylation of A_p by E: k_9,k_{9p} are the association-dissociation rates for the reaction intermediate $[A_pE]$, and ν_E is the rate of formation of A from this reaction intermediate.

Parameter values are based on [54], $k_1 = k_2 = k_3 = 1/(nM \cdot hr) = k_4 = k_5 = k_6 = k_7 = k_8 = k_9$,$k_{1p} = k_{2p} = k_{3p} = \nu_K = \nu_P = 10^3/hr = k_{4p} = k_{5p} = k_{6p} = k_{7p} = k_{8p} = k_{9p} = \nu_R = \nu_E$,$k_s = 10^2/hr$,$A_T = B_T = F_T = K_T = 1000nM$,$E_T = R_T = 100nM$ The steady state for different total concentrations of Spo0F is computed by numerically integrating these equations using ode23s (Supp. Fig. C.2e). For the computation with no reverse phosphotransfer, the corresponding rate constants are set to zero, $k_5 = k_7 = k_{4p} = k_{6p} = 0$. Similarly, for the computation with no Spo0F phosphatase, the corresponding parameters are set to zero, $R_T = k_8 = k_{8p} = \nu_R = k_3 = k_3p = \nu_P = 0$. In addition, there is an additional constraint as the reaction intermediate $[KTF_p]$ does not exist. Enforcing this constraint ($[KTF_p] = 0$) reduces the number of differential equations by one as the value of another reaction intermediate $[K_pF]$ is already determined, $[K_pF] = F_T - F - F_p - [F_pB] - [F_pR]$.

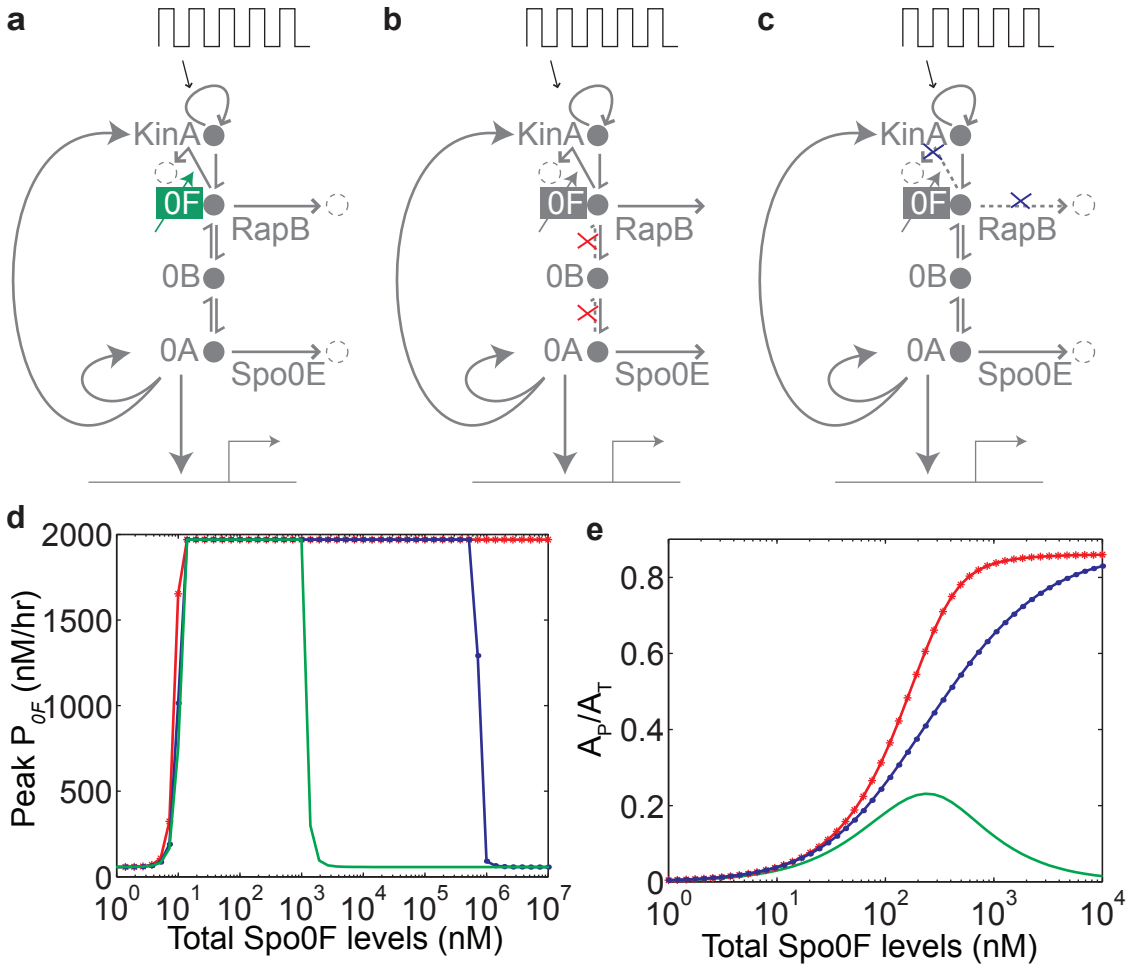

Figure C.2: Post-translational Spo0F bandpass in the full model with transcriptional feedback and pulsing or in the more complicated model of the core phosphorelay is due to the drain of Spo0A phosphates via reverse phosphotransfer and Spo0F phosphatase. Diagrams of the phosphorelay circuit (a) and versions with no reverse phosphotransfer (b, red) and no Spo0F phosphatase (c, blue), for which the post-translational Spo0F bandpass computation is performed from the full model described in the main text (including pulsing and transcriptional feedbacks, Fig. 2.7). Peak P_{0F} pulse amplitudes are plotted for different Spo0F induction levels (at steady state) for three cases: base parameters (d, green), no reverse phosphotransfer (d, red), and no Spo0F phosphatase (d, blue). The absence of Spo0F phosphatases shifts the repression threshold to significantly higher Spo0F values, representing drain of Spo0F phosphates by dilution due to cell growth. (e) Green curve is the post-translational Spo0F bandpass computed from a more complicated version of the core phosphorelay, described in the supplementary text. The computation is repeated in the absence of reverse phosphotransfer (red) and Spo0F phosphatases (blue).

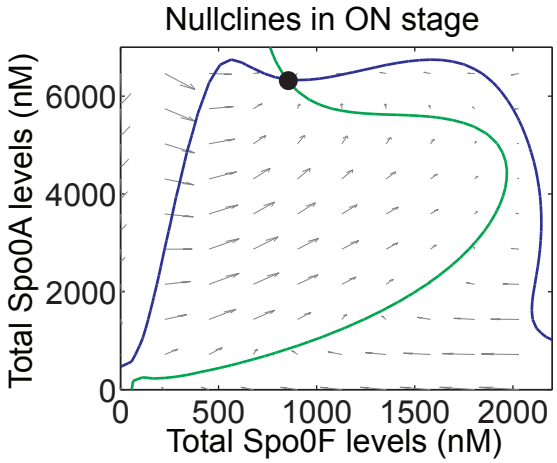

Figure C.3: Qualitative dynamic picture under the $P_{kinA} = P_{0A}$ assumption is similar to the alternate $P_{kinA} = P_{0F}$ assumption. Nullclines in the "ON" stage in the case when $P_{kinA}(A_p) = P_{0F}(A_p)$ are similar to the case discussed in 2.3 with the assumption that $P_{kinA}(A_p) = P_{0A}(A_p)$, suggesting that this assumption is justified. These nullclines are plotted for same parameters as used in the main text with $k_s(ON) = 110/hr$.

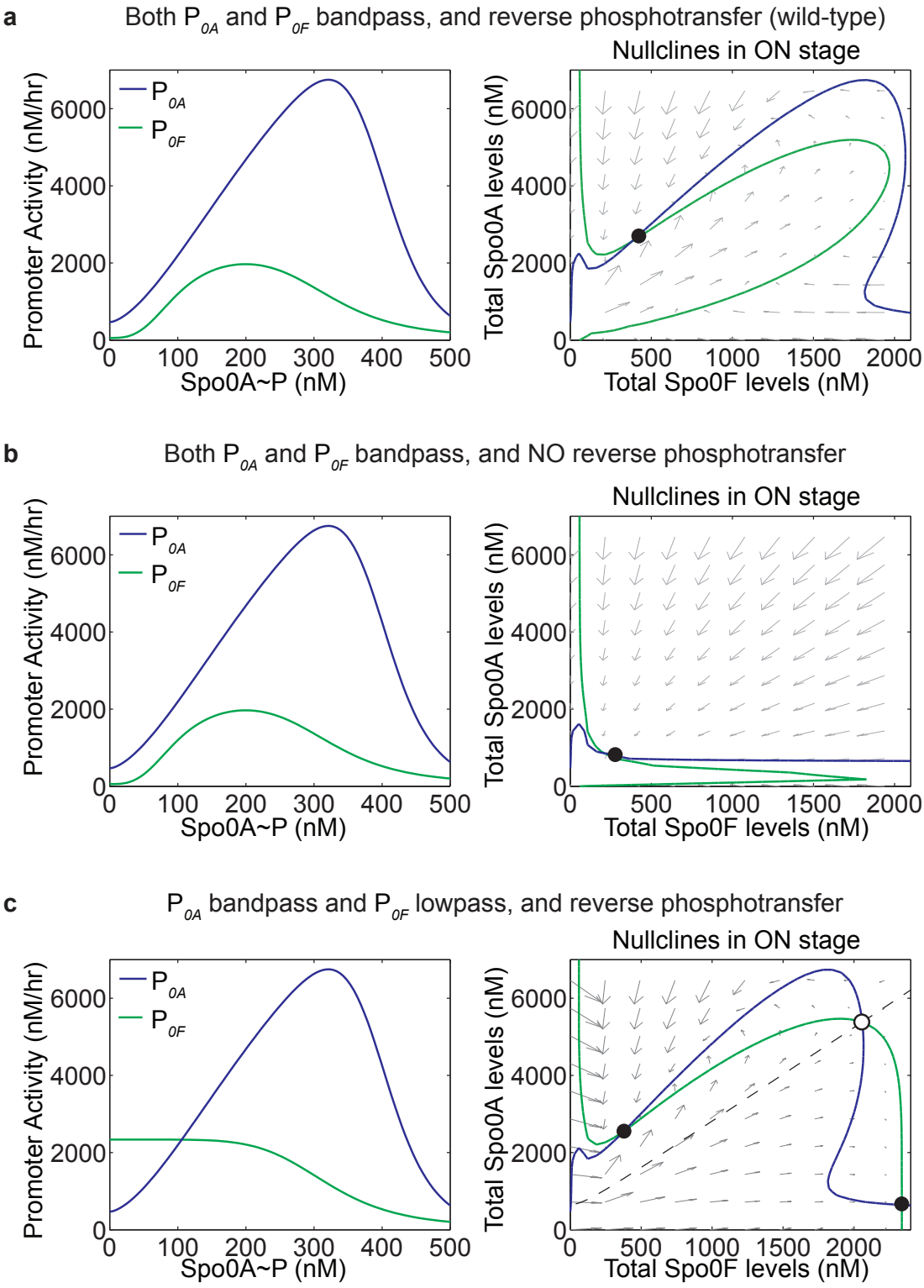
a
Both P0A and P0F bandpass, and reverse phosphotransfer (wild-type)
Nullclines in ON stage
P0A
P0F
Promoter Activity (nM/hr)
Spo0A~P (nM)
Total Spo0A levels (nM)
Total Spo0F levels (nM)
b
Both P0A and P0F bandpass, and NO reverse phosphotransfer
Nullclines in ON stage
c
P0A bandpass and P0F lowpass, and reverse phosphotransfer
Nullclines in ON stage

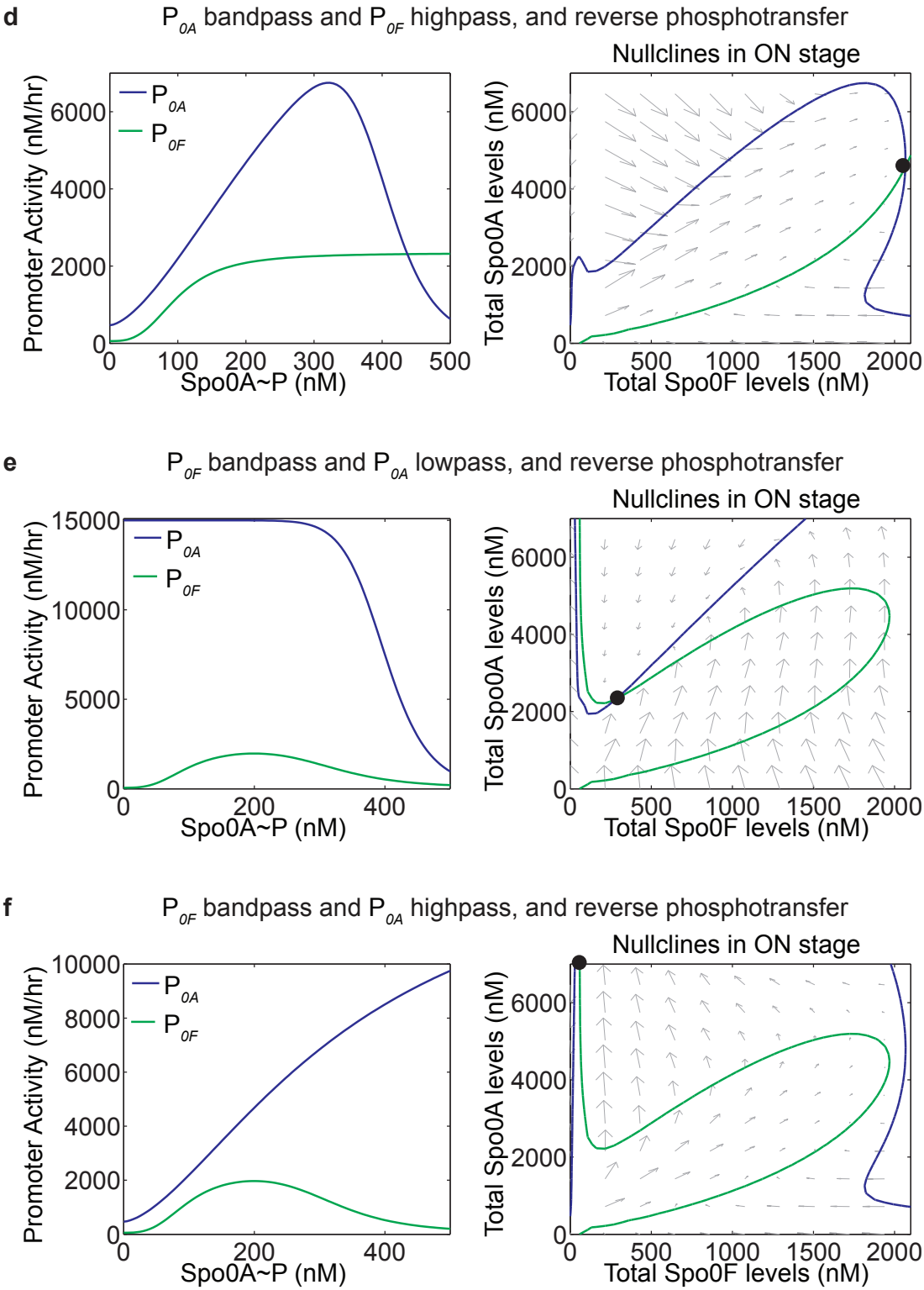
d
P0A bandpass and P0F highpass, and reverse phosphotransfer
Nullclines in ON stage
Promoter Activity (nM/hr)
Spo0A~P (nM)
Total Spo0A levels (nM)
Total Spo0F levels (nM)
P0A
P0F
e
P0F bandpass and P0A lowpass, and reverse phosphotransfer
Nullclines in ON stage
Promoter Activity (nM/hr)
Spo0A~P (nM)
Total Spo0A levels (nM)
Total Spo0F levels (nM)
P0A
P0F
f
P0F bandpass and P0A highpass, and reverse phosphotransfer
Nullclines in ON stage
Promoter Activity (nM/hr)
Spo0A~P (nM)
Total Spo0A levels (nM)
Total Spo0F levels (nM)
P0A
P0F

Figure C.4: Effect of bandpass characteristics on the alternate state. The effect of bandpass characteristics on the alternate state are investigated by comparing "ON" phase planes in the following cases, (a) Both P_{0A} and P_{0F} bandpass, and reverse phosphotransfer (wild-type case from Fig. 2.8, considered in 2.3) (b) Both P_{0A} and P_{0F} bandpass, and NO reverse phosphotransfer: Transcriptional bandpasses remain the same as case (a), but there is no post-translational bandpass. Nullclines orient differently from case (a), so that the alternate state doesn't exist and its effect on dynamics is minimal. (c) P_{0A} bandpass, P_{0F} lowpass (only repression), and reverse phosphotransfer: Nullclines are slightly perturbed from case (a), with the appearance of a stable steady state, an unstable steady state (white circle), and the associated separatrix. The separatrix is computed by integrating equations backward in time starting from an initial condition near the unstable steady state. The additional stable steady state is similar in location to the alternate state. (d) P_{0A} bandpass, P_{0F} highpass (only activation), and reverse phosphotransfer: Nullclines are slightly perturbed from case (a), with the stable steady state situated like the alternate state. (e) P_{0F} bandpass, P_{0A} lowpass (only repression), and reverse phosphotransfer: Nullclines are slightly perturbed from case (a), but without significant change in the steady state location. (f) P_{0F} bandpass, P_{0A} highpass (only activation) and reverse phosphotransfer: Nullclines are slightly perturbed from case (a), but without significant change in the steady state location. In this case, the stable steady state is situated above the upper Y-axes limit.

Bibliography

[1] B. Alberts. *Molecular biology of the cell*. Garland Science, 4th edition, 2002.

[2] E. Alm, K. Huang, and A. Arkin. The evolution of two-component systems in bacteria reveals different strategies for niche adaptation. *PLoS Comput Biol*, 2(11):1329–41, 2006.

[3] C. N. Anderson, C. H. Hsieh, S. A. Sandin, R. Hewitt, A. Hollowed, J. Beddingtom, R. M. May, and G. Sugihara. Why fishing magnifies fluctuations in fish abundance. *Nature*, 452(7189):835–9, 2008.

[4] E. Angelino and M. P. Brenner. Excitability constraints on voltage-gated sodium channels. *PLoS Comput Biol*, 3(9):1751–60, 2007.

[5] J. L. Appleby, J. S. Parkinson, and R. B. Bourret. Signal transduction via the multi-step phosphorelay: not necessarily a road less travelled. *Cell*, 86(6):845–48, 1995.

[6] S. Basu, Y. Gerchman, C. H. Collins, F. H. Arnold, and R. Weiss. A synthetic multicellular system for programmed pattern formation. *Nature*, 434(7037):1130–4, 2005.

[7] E. Batchelor and M. Goulian. Robustness and the cycle of phosphorylation and dephosphorylation in a two-component regulatory system. *Proc Natl Acad Sci USA*, 100(2):691–6, 2003.

[8] H. C. Berg. *Random walks in biology*. Princeton University Press, 1983.

[9] H. C. Berg. *E. coli in motion*. Springer, 2004.

[10] J. M. Berg, J. L. Tymoczko, and L. Stryer. *Biochemistry*. W. H. Freeman, 5th edition, 2002.

[11] M. J. Bick, V. Lamour, K. R. Rajashankar, Y. Gordiyenko, C. V. Robinson, and S. A. Darst. How to switch off a histidine kinase: crystal structure of *Geobacillus stearothermophilus* KinB with the inhibitor Sda. *J Mol Biol*, 386(1):163–77, 2009.

[12] D. Burbulys, K. A. Trach, and J. A. Hoch. Initiation of sporulation in *B. subtilis* is controlled by a multicomponent phosphorelay. *Cell*, 64(3):545–52, 1991.

[13] J. W. Chapman and P. J. Piggot. Analysis of the inhibition of sporulation of *Bacillus subtilis* caused by increasing the number of copies of the *spo0F* gene. *J Gen Microbiol*, 133(8):2079–88, 1987.

[14] L. J. Colwell and M. P. Brenner. Action potential initiation in the Hodgkin-Huxley model. *PLoS Comput Biol*, 5(1):1751–60, 2009.

[15] A. Csikasz-Nagy, L. Cardelli, and O. S. Soyer. Response dynamics of phosphorelays suggest their potential utility in cell signalling. *J R Soc Interface*, 8(57):480–88, 2011.

[16] T. Danino, O. Mondragón-Palomino, L. Tsimring, and J. Hasty. A synchronized quorum of genetic clocks. *Nature*, 426(7279):326–30, 2010.

[17] M. J. Dunlop, R. S. Cox 3rd, J. H. Levine, R. M. Murray, and M. B. Elowitz. Regulatory activity revealed by dynamic correlations in gene expression noise. *Nat Genet*, 40(12):1493–8, 2008.

[18] H. El-Samad, H. Kurata, J. Doyle, C. Gross, and M. Khammash. Surviving heat-shock: control strategies for robustness and performance. *Proc Natl Acad Sci USA*, 102(8):2736–41, 2005.

[19] A. Eldar, V. K. Chary, P. Xenopoulos, M. E. Fontes, O. C. Loson, J. Dworkin, P. J. Piggot, and M. B. Elowitz. Partial penetrance facilitates developmental evolution in bacteria. *Nature*, 460(7254):510–4, 2009.

[20] M. B. Elowitz and S. Leibler. A synthetic oscillatory network of transcriptional regulators. *Nature*, 403(6767):335–8, 2000.

[21] A. S. Forouhar, M. Liebling, A. Hickerson, A. Nasiraei-Moghaddam, H. J. Tsai, J. R. Hove, S. E. Fraser, M. E. Dickinson, and M. Gharib. The embryonic vertebrate heart tube is a dynamic suction pump. *Science*, 312(5774):751–3, 2006.

[22] M. Fujita, J. E. Gonzalez-Pastor, and R. Losick. High- and low-threshold genes in the Spo0A regulon of *Bacillus subtilis*. *J Bacteriol*, 187(4):1357–68, 2005.

[23] M. Fujita and R. Losick. Evidence that entry into sporulation in *Bacillus subtilis* is governed by a gradual increase in the level and activity of the master regulator Spo0A. *Genes Dev*, 19(18):2236–44, 2005.

[24] M. Fujita and Y. Sadaie. Feedback loops involving Spo0A and AbrB in *in vitro* transcription of the genes involved in the initiation of sporulation in *Bacillus subtilis*. *Biochem*, 124(1):98–104, 1998.

[25] T. S. Gardner, C. R. Cantor, and J. J. Collins. Construction of a genetic toggle switch in *Escherichia coli*. *Nature*, 403(6767):339–42, 2000.

[26] D. Georgellis, O. Kwon, and E. C. Lin. Quinones as the redox signal for the arc two-component system of bacteria. *Science*, 292(5522):2314–6, 2001.

[27] S. F. Gilbert and S. R. Singer. *Developmental biology*. Sinauer Associates ; NCBI, 6th edition, 2000.

[28] C. E. Grimshaw, S. Huang, C. G. Hanstein, M. A. Strauch, D. Burbulys, L. Wang, J. A. Hoch, and J. M. Whiteley. Synergistic kinetic interactions between components of the phosphorelay controlling sporulation in *Bacillus subtilis*. *Biochemistry*, 37(5):1365–75, 1998.

[29] James A. Hoch and Thomas J. Silhavy, editors. *Two-component signal transduction*. ASM Press, 1995.

[30] K. C. Huang, Y. Meir, and N. S. Wingreen. Dynamic structures in *Escherichia coli*: Spontaneous formation of MinE rings and MinD polar zones. *Proc Natl Acad Sci USA*, 100(22):12724–8, 2003.

[31] K. Ireton, D. Z. Rudner, K. J. Siranosian, and A. D. Grossman. Integration of multiple developmental signals in *Bacillus subtilis* through the Spo0A transcription factor. *Genes Dev*, 7(2):283–94, 1993.

[32] J. P. Keener and J. Sneyd. *Mathematical physiology*. Springer, 1998.

[33] J. R. Kim and K. H. Cho. The multi-step phosphorelay mechanism of unorthodox two-component systems in *E. coli* realizes ultrasensitivity to stimuli while maintaining robustness to noises. *Comput Biol Chem*, 30(6):438–44, 2006.

[34] B. A. Krizek and J. C. Fletcher. Molecular mechanisms of flower development: an armchair guide. *Nat Rev Genet*, 6(9):688–98, 2005.

[35] J. H. Levine and M. B. Elowitz. Manuscript under review.

[36] M. Liebling, A. S. Forouhar, R. Wolleschensky, B. Zimmermann, R. Ankerhold, S. E. Fraser, M. Gharib, and M. E. Dickinson. Rapid three-dimensional imaging and analysis of the beating embryonic heart reveals functional changes during development. *Dev Dyn*, 235(11):2940–8, 2006.

[37] J. C. Locke and M. B. Elowitz. Using movies to analyse gene circuit dynamics in single cells. *Nat Rev Microbiol*, 7(5):383–92, 2009.

[38] I. Mihalescu, W. Hsing, and S. Leibler. Resilient circadian oscillator revealed in individual cyanobacteria. *Nature*, 430(6995):81–5, 2004.

[39] W. Min and X. S. Xie. Kramers model with a power-law friction kernel: Dispersed kinetics and dynamic disorder of biochemical reactions. *Physical Review E*, 73(1):010902, 2006.

[40] J. D. Murray. *Mathematical biology*. Springer, 3rd edition, 2002.

[41] I. Nachman, A. Regev, and S. Ramanathan. Dissecting timing variability in yeast meiosis. *Cell*, 131(3):544–56, 2007.

[42] E. M. Ozbudak, M. Thattai, H. N. Lim, B. I. Shraiman, and A. v. Oudenaarden. Multistability in the lactose utilization network of *Escherichia coli*. *Nature*, 427(6976):737–40, 2004.

[43] M. Perego, C. Hanstein, K. M. Welsh, T. Djavakhishvili, P. Glaser, and J. A. Hoch. Multiple protein-aspartate phosphatases provide a mechanism for the integration of diverse signals in the control of development in *B. subtilis*. *Cell*, 79(6):1047–55, 1994.

[44] M. Perego and J. A. Hoch. Isolation and sequence of the *spo0E* gene: its role in initiation of sporulation in bacillus subtilis. *Mol Microbiol*, 1(1):125–32, 1987.

[45] M. Perego and J. A. Hoch. Negative regulation of *Bacillus subtilis* sporulation by the *spo0E* gene product. *J Bacteriol*, 173(8):2514–20, 1991.

[46] P. J. Piggot and D. W. Hilbert. Sporulation of *Bacillus subtilis*. *Curr Opin Microbiol*, 7(6):579–86, 2004.

[47] Mark Ptashne. *A genetic switch : phage lambda revisited*. Cold Spring Harbor Laboratory Press, 3rd edition, 2004.

[48] M. Qi and E. A. Elion. Map kinase pathways. *J Cell Sci*, 118(16):3659–72, 2005.

[49] G. V. Reddy, S. P. Gordon, and E. M. Meyerowitz. Unravelling developmental dynamics: transient intervention and live imaging in plants. *Nat Rev Mol Cell Biol*, 8(6):491–501, 2007.

[50] I. H. Riedel-Kruse, C. Müller, and A. C. Oates. Synchrony dynamics during initiation, failure, and rescue of the segmentation clock. *Science*, 317(5846):1911–15, 2007.

[51] F. D. Russo and T. J. Silhavy. The essential tension: opposed reactions in bacterial two-component regulatory systems. *Trends Microbiol*, 1(8):306–10, 1993.

[52] M. J. Rust, J. S. Markson, W. S. Lane, D. S. Fisher, and E. K. O'Shea. Ordered phosphorylation governs oscillation of a three-protein circadian clock. *Science*, 318(5851):809–12, 2007.

[53] S. Sen and M. Elowitz. Phosphotransfer in two-component signal transduction can enhance range of sensitivity. Poster, Gordon Research Conference on Microbial Adhesion and Signal Transduction, 2007.

[54] G. Shinar, R. Milo, M. R. Martinez, and U. Alon. Input-output robustness in simple bacterial signaling systems. *Proc Natl Acad Sci USA*, 104(50):19931–5, 2007.

[55] S. L. Spencer, S. Gaudet, J. G. Albeck, J. M. Burke, and P. K. Sorger. Non-genetic origins of cell-to-cell variability in TRAIL-induced apoptosis. *Nature*, 459(7245):428–32, 2009.

[56] A. M. Stock, V. L. Robinson, and P. N. Goudreau. Two-component signal transduction. *Annu Rev Biochem*, 69:183–215, 2000.

[57] J. Stricker, S. Cookson, M. Bennett, W. Mather, L. Tsimring, and J. Hasty. A fast, robust and tunable synthetic gene oscillator. *Nature*, 456(7221):516–9, 2008.

[58] G. M. Suel, J. Garcia-Ojalvo, L. M. Liberman, and M. B. Elowitz. An excitable gene regulatory circuit induces transient cellular differentiation. *Nature*, 440(7083):545–50, 2006.

[59] G. M. Suel, R. P. Kulkarni, J. Dworkin, J. Garcia-Ojalvo, and M. B. Elowitz. Tunability and noise dependence in differentiation dynamics. *Science*, 315(5819):1716–9, 2007.

[60] L. Swint-Kruse and K. S. Mathews. Allostery in the LacI/GalR family: variations on a theme. *Curr Opin Microbiol*, 12(2):129–37, 2009.

[61] J. W. Veening, L. W. Hamoen, and O. P. Kuipers. Phosphatases modulate the bistable sporulation gene expression pattern in *Bacillus subtilis*. *Mol Microbiol*, 56(6):1481–94, 2005.

[62] J. W. Veening, H. Murray, and J. Errington. A mechanism for cell cycle regulation of sporulation initiation in *Bacillus subtilis*. *Genes Dev*, 23(16):1959–70, 2009.

[63] F. Wellmer, M. Alves-Ferreira, A. Dubois, J. L. Riechmann, and E. M. Meyerowitz. Genome-wide analysis of gene expression during early *Arabidopsis* flower development. *PLoS Genet*, 2(7):e117, 2006.

[64] A. T. Winfree. *The geometry of biological time*. Springer, 2nd edition, 2001.

[65] K. Wuichet, B. J. Cantwell, and I. B. Zhulin. Evolution and phyletic distribution of two-component signal transduction systems. *Curr Opin Microbiol*, 13(2):219–25, 2010.

[66] W. Xiong and J. E. Ferrell Jr. A positive-feedback-based bistable "memory module" that governs a cell fate decision. *Nature*, 426(6965):460–5, 2003.

[67] T.-M. Yi, Y. Huang, M. I. Simon, and J. Doyle. Robust perfect adaptation in bacterial chemotaxis through integral feedback control. *Proc Natl Acad Sci USA*, 97(9):4649–53, 2000.

[68] A. Zaslaver, A. E. Mayo, R. Rosenberg, P. Bashkin, H. Sberro, M. Tsalyuk, M. G. Surette, and U. Alon. Just-in-time transcription program in metabolic pathways. *Nat Genet*, 36(5):486–91, 2004.